Lawrence Berkeley National Laboratory
Lawrence Berkeley National Laboratory

Title
HEAVY ION COLLISIONS AT RELATIVISTIC ENERGIES

Permalink
https://escholarship.org/uc/item/9578m83r

Author
Nagamiya, S.

Publication Date
1979-07-01

Peer reviewed

eScholarship.org Powered by the California Digital Library
University of California

NOTICE
This report was prepared as an account of work sponsored by the United States Government. Neither the United States nor the United States Department of Energy, nor any of their employees, nor any of their contractors, subcontractors, or their employees, makes any warranty, express or implied, or assumes any legal liability or responsibility for the accuracy, completeness or usefulness of any information, apparatus, product or process disclosed, or represents that its use would not infringe privately owned rights.

HEAVY ION COLLISIONS AT RELATIVISTIC ENERGIES

Shoji Nagamiya

Lawrence Berkeley Laboratory, University of California
Berkeley, California 94720

1. INTRODUCTION

About five years ago a summer study was held in Berkeley on relativistic heavy-ion collisions.[1] Several stimulating theoretical suggestions were reported there on the possibility of creating a highly-excited, dense nuclear system by using relativistic heavy-ion beams. These suggestions have greatly encouraged experimentalists and, in fact, have had a strong influence on the experimental programs pursued in the last few years.

So far, however, no concrete experimental evidence of the existence of dense nuclear matter has been observed. In this regard, the major question addressed by relativistic heavy-ion research has not been answered at the present stage, and it remains for future experimental and perhaps theoretical investigations.

Instead, the most exciting and fruitful results of the last few years can be found in the pursuit of a deep understanding of the basic reaction mechanism. In this regard there has been a strong interplay between experimental data and theoretical analysis which has created promising results. The major interests are related to (1) geometry and (2) dynamics of the collisions. In the first part of this paper the current understanding of the reaction mechanism is reviewed and described.

Recent measurements have also revealed some new phenomena which cannot be easily explained within the framework of the available theoretical tools.

These phenomena observed with beam energies of 0.4 - 2 GeV/A are described in the second part of this paper, as those observed with beams below a few 100 MeV/A will be reported by other speakers.[2]

In the last part of the paper, the topics remaining for future studies are briefly mentioned, especially in connection with the present conference's subject, namely, as study of collisions at beam energies of 10 - 200 MeV/A.

2. COLLISION GEOMETRY

Typical examples of fragment spectra in relativistic nuclear collisions are shown in Figs. 1 and 2. Fig. 1 displays the data by Anderson et al.[3] who measured p, d, t, and ^{3}He at $\theta_{Lab} = 0°$ in collisions of 2.1 GeV/A α + C. The yield of each fragment is sharply peaked at a certain momentum. If we plot these data as a function of the relativistic-invariant velocity called the rapidity y, which is defined as

$$y \equiv \frac{1}{2} \ln[(1 + p_{//}/E)/(1 - p_{//}/E)], \qquad (1)$$

then all the fragments have a peak at the same rapidity which is almost the same as the beam rapidity, y_B. This implies that most of the fragments at 0° came from a piece of the beam nucleus which was not scraped out by the target nucleus. Thus the velocity of this piece is the same as the beam velocity. Furthermore, the mass (A) and charge (Z) of the beam fragments are always smaller than those of beam nucleus, (A_B, Z_B). Two features, y (at peak) $\simeq y_B$ and $(A,Z) \leq (A_B, Z_B)$, are commonly observed for fragments emitted at 0° in all combinations of beam and target nuclei, as have already been shown by Heckman et al.[4,5] and by Papp et al.[6]

Fragment emission at large angles is somewhat different. Fig. 2 shows

proton inclusive spectra at large angles (θ_{Lab} = 10° - 145°), observed in collisions of 800 MeV/A Ar + KCl. There the spectra are essentially structureless and very smooth as a function of laboratory momentum. The dominant yield at large angles comes from protons (≥ 60 - 70 % of total yield).

These two observations readily suggest a simple picture of the collision geometry, as shown in Fig. 3. This is called the participant-spectator model. After the collision the non-overlapping part between beam and target nuclei, called the spectator, just keeps going without any interference. On the other hand, in the overlap region, called the participant region, strong interactions occur between nucleons of beam and target, with the result that the fragments are emitted over a wide angular range. The fragments from the participant piece are mainly elementary particles such as protons, neutrons, or pions, because the energy transfer involved there is much higher than the mutual binding energies of the nucleons.

The average number of participant protons which come from the beam nucleus, $\langle Z_{Beam}^{Participant} \rangle$, is proportional to the ratio of the target cross section to the total cross section,

$$\langle Z_{Beam}^{Participant} \rangle = Z_B \frac{\pi (r_0 A_T^{1/3})^2}{\pi (r_0 A_B^{1/3} + r_0 A_T^{1/3})^2}$$

$$= Z_B A_T^{2/3} / (A_B^{1/3} + A_T^{1/3})^2 \quad . \qquad (2)$$

Similarly, we have

$$\langle Z_{Target}^{Participant} \rangle = Z_T A_B^{2/3} / (A_B^{1/3} + A_T^{1/3})^2 \quad . \qquad (3)$$

The total nuclear charge of the beam fragments is thus given by

$$\underbrace{(Z_B - \langle Z_{Beam}^{Participant} \rangle)}_{\text{Beam spectator charge}} \times \underbrace{\pi r_0^2 (A_B^{1/3} + A_T^{1/3})^2}_{\text{Cross section}}$$

$$= \pi r_0^2 Z_B (A_B^{2/3} + 2A_B^{1/3} A_T^{1/3}). \tag{4}$$

On the other hand, the total nuclear charge emitted from the participant piece becomes

$$(\langle Z_{Beam}^{Participant} \rangle + \langle Z_{Target}^{Participant} \rangle) \times \pi r_0^2 (A_B^{1/3} + A_T^{1/3})^2$$
$$= \pi r_0^2 (Z_B A_T^{2/3} + Z_T A_B^{2/3}) \ . \tag{5}$$

Formula (4) is given by Hüfner et al.[7]

In Figs. 4 and 5 the formulas (4) and (5) are tested. For beam fragments the experimental points shown in Fig. 4 were calculated from the data by Lindstrom et al.[4] who measured all isotope yields at 0° for beams of C and O. The target mass (A_T) dependence of the yield goes like A_T^n where $n \sim 1/4$. This is predicted in Eq. (4). The absolute values predicted by Eq.(4) are about 50% larger than the observed yields. This may be due to missing charges which have not been detected in the experiment, or it may be a result of the crude assumptions used to derive Eq. (4). In spite of this 50% discrepancy, we can conclude that the simple geometrical picture explains very well the beam fragments.

Fig. 5 shows the sum of charges for p, d, t, and ^{3}He calculated from the data at large angles. In order to obtain the total yield an extrapolation to 0° and 180° was done based on the data at $10° < \theta < 145°$. The ambiguity of the extrapolation is not large, since $(d\sigma/d\theta)_{0°} = (d\sigma/d\theta)_{180°} = 0$. The yield plotted in this figure comes most likely from the participant piece. Agreement of the data with the prediction by Eq. (5) is fair.

A similar argument can be made for target fragments. However, no precise data for target fragments are available, because it is almost impossible to measure all isotopes produced as target fragments. Extensive measurements of

unstable isotope production were recently reported,[8] and it may be worthwhile to extrapolate these data to stable isotopes and to compare the results with Eq. (3).

From the comparison described above we can conclude that the geometrical aspect of heavy-ion collisions at relativistic energies can be explained rather well with a simple picture, the participant-spectator model. In the use of this model it is rather instructional to know that about 1/4 of the total available nuclear charges go into forming the participant region in the case of identical nucleus collisions, since the yield of the participant charges is given by $2\pi r_0^2 ZA^{2/3}$ while that of spectator charges (beam + targets spectators) is given by $6\pi r_0^2 ZA^{2/3}$

Once the geometry is understood, the next immediate interest is the dynamics. In the next section the dynamics for the participant is discussed.

3. COLLISION DYNAMICS FOR PARTICIPANT REGION

3.1 Inclusive Proton and Pion Spectra

Consider the nucleus-nucleus collision to be simply a superposition of nucleon-nucleon scatterings. At relativistic energies the mean free path of nucleons inside the nucleus is 1 - 2 fm, which is shorter than the typical nuclear radius. This implies that both the single nucleon-nucleon knock-out and multiple nucleon cascades contribute to the production of fragments. The particle yield, σ, can thus be written as

$$\sigma = \sum_{i=1}^{\infty} \sigma_i \ , \qquad (6)$$

where σ_i describes the yield of particles emitted after i-th nucleon-nucleon scatterings. The $i = 1$ term expresses the clean knock-out (hereafter called

the CKO) process. If the terms with large i's are dominant compared to others, namely if particles are emitted after a sufficiently large number of nucleon-nucleon scatterings, statistical models, such as the thermal model, become more accurate in predicting the yields. In this section we will consider which of σ_i's are dominant in relativistic heavy-ion collisions.

For this purpose the first step is to compare the inclusive data with the theoretical prediction for each of the σ_i terms. For simplicity we usually restrict our considerations to identical nucleus collisions except in places where other combinations between beam and target nuclei play a key role in the discussion.

Theoretically two extreme cases are easily handled: the CKO process (σ_1),[9,10,11] and the thermal process ($\sum_{i=m}^{\infty} \sigma_i$; m:large).[12,13,14] According to the thermal model, the total available energy in the participant region will be converted to thermal energy, giving a temperature, T, which is given by[13]

$$E_B^*/A = \frac{3}{2} T + 2.28 \frac{\rho_0}{\rho} \left(\frac{T}{m_\pi c^2}\right)^{9/2} m_\pi c^2, \qquad (7)$$

where E_B^*/A is the c.m. kinetic energy of the incident beam per nucleon, and ρ is the nuclear density of the participant piece. Once the energy per nucleon is fixed, then the temperature is independent of the mass number of the incident beam nucleus. [The above formula is valid for identical nucleus collisions.]

Fig. 6 shows the energy spectra of protons at c.m. 90° for collisions of C + C, Ne + NaF, and Ar + KCl at E_{Beam} = 800 MeV/A, all of which are essentially identical nucleus collisions. The c.m. 90° spectra were selected, since the particle emission at this angle is less affected by the spectator fragments. The shape of energy spectra is exponential at high energies but deviates substantially from an exponential at low energies.

The exponential shape is expected from the thermal model, since this model predicts a Boltzman distribution. The exponential slopes for the three spectra are almost independent of the nuclear masses, which is what we expect from Eq. (7). At E_{Beam}(Lab) = 800 MeV/A, E_B^*/A = 182 in Eq. (7), which gives T = 91 MeV for $\rho_0/\rho = 1$ and T = 82 MeV for $\rho_0/\rho = 2$. If we use T = 82 MeV and apply the participant-spectator model (given by Eq. (5)) for the purpose of absolute normalization, then the theoretical curve for collisions of Ne + NaF roughly explains the observed data to within a factor of 2-3, as shown by a thick solid curve in Fig. 6. Here, the isotropic angular distribution is assumed to derive the theoretical curve. The mass dependence of the observed yield, $(d\sigma/d\Omega)_{90°}$, is roughly given by

$$\left(\frac{d\sigma}{d\Omega}\right)_{90°}^{\text{protons}} \propto Z^n \qquad \text{with } n = 1.9 \pm 0.3, \tag{8}$$

which is predicted from Eq. (5), where n is 5/3 = 1.67.

Next, let us study the prediction of the CKO model. If we neglect the internal motion of nucleons inside the nucleus, elastically scattered protons should be sharply peaked at $E_p^* = E_B^*/A$ = 182 MeV. Inelastic pp or pn scatterings produce protons with lower energies than this. However, the actual nucleons have an internal motion called Fermi motion. Hatch and Koonin[11] used an empirical form of the momentum distribution of nucleons inside the nucleus, derived by Frankel et al.,[14] as

$$\frac{d^3f}{d^3\vec{p}} \propto (|\vec{p}|/p_0)/\sinh(|\vec{p}|/p_0), \tag{9}$$

and calculated the proton spectra. The results are indicated by a dashed curve in Fig. 6. The slope is nearly exponential, and of course, by definition, the slope does not depend on the mass of the colliding nuclei. The assumption of the momentum distribution of the form of Eq. (9) has to be

carefully examined,* but, nevertheless, the surprising fact is that the σ_1 term can again explain the dominant feature of the proton energy spectrum at almost the same level that the thermal model did. If we change the value of p_0 to a larger value, the agreement becomes even better.

Now we face a dilemma: both models predict almost the same tendency for the energy spectra. In the rest of this subsection we will therefore compare other aspects of inclusive data with both the thermal and CKO models.

Fig. 7 shows proton and pion energy spectra at c.m. angle of 90° in collisions of 800 MeV/A Ne + NaF. We observe that the exponential slope of pions is steeper than that of protons. The thermal model predicts the same slope for pions. We therefore first thought that a comparison between protons and pions would tell us the importance of the CKO process. However, the situation is not so simple. As pointed out by Kapusta[17] the decay characteristics of the Δ-resonance induces a steeper slope for pions than the calculated slope without Δ's. Recently Sano et al.[18] noticed this point and showed that the pion slope is steeper than the proton slope if we take into account a stronger Δ effect, as shown in the figure. An alternative explanation based on the thermal model was presented by Siemens and Rasmussen[19] who proposed an explosion flow (blast wave) from the compressed nuclear matter. I personally feel that this model is very attractive. However, the point here is that both thermal and CKO models can again predict the observed difference between proton and pion slopes.

In Fig. 8 we show the beam energy dependence of the proton spectra in collisions of Ne + NaF. The slope strongly depends on the beam energy. However, if we plot these observed slopes in Fig. 9, then both thermal and

*This point will be discussed later in Sec. 4.3.

CKO models again explain reasonably well the observed slopes. Here, the slope was estimated by Eq. (7) for the thermal model and by our Monte Carlo calculations for the CKO model. In the CKO model the high energy protons are produced mainly by the high-momentum component of the Fermi motion. As the beam energy is increased, such a component is enhanced more than the linear sum, $\vec{p}_F + \vec{p}_{c.m.}$, because of the relativistic effect.

The yield of protons and pions at c.m. 90°, $(d\sigma/d\Omega)_{90°}$, predicted by both models are compared with the data in Fig. 10. Within the framework of the thermal model, the proton yield stays constant because it is determined solely by the number of participant protons and independent of the kinematics. On the other hand, the CKO process directly reflects the kinematics of nucleon-nucleon scatterings, and we expect less yield at 90° for high energy beams. Nevertheless, the dominant features can be explained reasonably well by both the models. In regard to pions, dynamics determines their yield in both models. In the thermal model the ratio of the π^- to proton yield is expressed as[13,14]

$$\frac{N_{\pi^-}}{N_p} \simeq 0.46 \frac{\rho_0}{\rho} \left(\frac{T}{m_\pi c^2}\right)^4$$
$$= 0.2 \left[\frac{E_B^*}{A} \frac{1}{\sqrt{m_\pi c^2 T}} - \frac{3}{2}\sqrt{\frac{T}{m_\pi c^2}}\right] , \qquad (10)$$

whereas the CKO process using the Δ-isobar model predicts

$$\left(\frac{N_{\pi^-}}{N_p}\right)_{\Delta\text{-model}} = \frac{1}{2} \frac{\frac{5}{6}\left(\frac{d\sigma}{d\Omega}\right)^{\text{inel}}_{pp} + \frac{1}{3}\left(\frac{d\sigma}{d\Omega}\right)^{\text{inel}}_{pn}}{\left(\frac{d\sigma}{d\Omega}\right)^{\text{total}}_{pp} + \left(\frac{d\sigma}{d\Omega}\right)^{\text{total}}_{pn}} \qquad (11)$$

for identical-mass nuclear collisions. Here the angular distribution of inelastically scattered protons is assumed to be the same as that of pions.

For a 2.1 GeV/A beam, not only Δ but some other excited nuclear states, such as N* and ρ, are produced as well, which cause the multipion emission. Using an empirical pion multiplicity per nucleon-nucleon inelastic scattering,[20] we approximated the ratio as

$$\frac{N_{\pi^-}}{N_p} \simeq M \cdot \left(\frac{N_{\pi^-}}{N_p}\right)_{\Delta\text{-model}} , \qquad (12)$$

where M = 1 for 400 and 800 MeV/A and M = 1.44[20] for 2.1 GeV/A. The predictions of Eqs. (10) and (12) again fit the data well.

As the last piece of information from the inclusive spectra, the angular distributions of protons in the c.m. frame are shown in Fig. 11. Shown here are those for protons with c.m. energies of 200, 400, and 600 MeV emitted in the collisions of 800 MeV/A Ar + KCl. How we observe for the first time a sharp difference between the predictions of the two models. The data show in general the forward and backward peaking, but the ratio of forward to 90° yield is not as large as the prediction of the CKO model. The thermal model should show an isotropic distribution, because there the multiple collisions are dominant, and all the initial memory of the beam direction is lost. The data certainly deviate from it. In this respect both predictions fail to explain the data, and it is strongly suggested that the inclusive data are a mixture of the two components, thermal and CKO processes.

In summary, the inclusive data show the following features:

(1) Several aspects of the energy spectra at c.m. 90°, especially their shape, the slope difference between protons and pions, and the beam energy dependence can be explained by both the thermal and CKO models.

(2) The angular distribution cannot be explained by either model. The data strongly suggest that both components make large contributions to the inclusive data.

Regarding the second point, several models which effectively include both aspects have been developed,[16,21,22] including the very complicated cascade calculations.[23,24] However, in the following two subsections, further studies on the roles of CKO and thermal components will be described from an experimental point of view.

3.2 Two-Proton Correlations

The experimental layout is sketched in Fig. 12. In addition to the magnetic spectrometer (S), which has been used to measure inclusive data, three sets of tag counter telescopes were prepared. These tag counters, named right (R), up (U) and down (D) counters, were set at angles (θ,ϕ) = (40°, 180°), (40°, 90°), and (40°, 270°), respectively, the beam axis being the z-axis. This θ-angle corresponds to $\theta_{c.m.} \sim 90°$ in the nucleon-nucleon c.m. frame. The spectrometer was located at $\phi = 0°$ and rotated between $\theta = 15°$ and 110°. With each telescope protons with energies $E_p > 200$ MeV, and occasionally $E_p > 100$ MeV, were detected. The solid angle of each telescope was 48 msr which subtended angles $35° < \theta < 45°$.

We take the ratio $C(\theta,p)$ defined as

$$C(\theta,p) \equiv 2\,\frac{(S(\theta,p)\cdot R)/R}{(S(\theta,p)\cdot U)/U + (S(\theta,p)\cdot D)/D}\,, \qquad (13)$$

where θ and p are the scattering angle and momentum of a proton detected in the spectrometer. The quantity $(S(\theta,p)\cdot R)$ indicates the coincidence counts between the spectrometer and R-telescope, and R indicates the single counts of the R-telescope. The ratio C then can be called the degree of coplanarity,

because, if $C > 1$, then the coplanar-type two-proton emission is favored. In the thermal limits we expect $C \approx 1$.

In Fig. 13 contour lines of the observed values of $C(\theta,p)$ are shown for collisions of C + C and Ar + KCl at E_{Beam} = 800 MeV/A. The data are displayed in the plane of $p_{\parallel}^{*}$ and $p_{\perp}$ of the emitted protons in the nucleon-nucleon c.m. frame. The dotted circle indicates the nucleon-nucleon elastic scattering kinematics when the internal motion of nucleons inside the nucleus is ignored. In the case of C + C the value of C is always larger than 1, and C has a peak right on the circle but at the opposite side of the intersection between the R-telescope and the circle. Here, the cross-hatched area shows the kinematical region of protons detected by the R-telescope. The data thus clearly show the existence of p-p quasi-elastic scattering.

The broadening of the peak is due to the Fermi-motion. The shape and width of C can be fitted by both the Gaussian and exponential shapes of internal momentum distributions with $\langle p_F \rangle \sim 260$ MeV/c. A typical fit is shown in Fig. 14.

The peak height is higher for C + C than for Ar + KCl. One can guess that this may be because the fraction of the CKO process is larger for a lighter mass system. However, such a guess is not quite correct. In order to explain it let us consider the extreme case where all protons are produced from purely CKO elastic scatterings, as shown in Fig. 15. When both the beam and target are protons, then the two scattered protons are completely correlated so that $C = \infty$. If the beam and target are both diprotons, then there are two pairs of p-p elastic scatterings. In each pair the two protons are correlated, but since there is no correlation between the pairs, the U- or D-counter can be fired even when one proton is detected by the

spectrometer, so that C is now finite. When there are two pairs of p-n elastic scatterings, two protons come from two independent elastic scatterings so that C = 1. A nucleus-nucleus collision is the sum of all possible combinations. When sufficiently large numbers of pairs are involved, we can derive the following relation:

$$(C - 1)_{\text{at peak}} \propto 1/\langle Z \rangle \ , \tag{14}$$

where $\langle Z \rangle$ is the average proton number involved in the system. Therefore, the value C could be smaller for the system with a larger number of protons.

In actual nuclear collisions both inelastic and elastic scatterings are invloved in the CKO process, which makes the ratio C even smaller. Define the fraction of the CKO component, P, as

$$P \equiv \sigma_1 / \sum_{i=1}^{\infty} \sigma_i = \sigma_1 / \sigma \ . \tag{15}$$

Then P is proportional to the probability of finding one proton emitted by a single CKO process. For two-proton correlations the probability of finding two protons, both of which are emitted by a single CKO process, is proportional to P^2. We then can easily guess

$$(C - 1)_{\text{at peak}} \propto P^2/\langle Z \rangle \ . \tag{16}$$

The actual formula of (C - 1) in terms of P and $\langle Z \rangle$ is slightly more complicated. Calculated results for collisions of identical nuclei at E_{Beam} = 800 MeV/A are plotted in Fig. 16 as a function of the average charged-particle multiplicity, m_T. Curves are labeled according to the percentage values of P. Cross-hatched areas indicate experimental points obtained in C + C, Ne + NaF, and Ar + KCl. Experimental values of m_T, which now include both π^+ and π^-, were determined from the total inclusive yield divided by

the geometrical cross section. From the figure we conclude

$$P \sim 50\% \tag{17}$$

for all the combinations of beam and target nuclei. This implies that, for protons emitted at $\theta_{c.m.} \sim 90°$ with the energy $E_p^* = E_B^*/A$, half are from a single CKO process. For Ne + NaF at $E_{Beam(Lab)} = 400$ MeV/A our results again show $P \sim 50\%$. Two-proton correlation measurements are thus very useful for evaluating the fraction of a CKO process for protons emitted in a limited kinematical region.

Another interesting feature observed in two-proton correlations is the anti-coplanarity for heavy-mass targets. Fig. 17 shows the contour plot of C for the collisions of 800 MeV/A C + Pb. The ratio C is smaller than 1, and, furthermore, we observe a valley of contour lines which tends toward $\theta_{c.m.} \sim 60°$. This phenomenon can qualitatively be understood in terms of nuclear shadowing, as illustrated in Fig. 17. When we detect the first particle at a certain angle, then the reaction region is effectively biased toward the shaded hemisphere shown in Fig. 17. In this case, it is rather difficult for the second particle to be emitted in the opposite direction from the first, because it has to penetrate the thick nuclear matter. On the other hand, it is not very difficult for the second particle to be emitted in the up or down direction. This makes $C < 1$.

3.3 High-Multiplicity Events

High-multiplicity events (hereafter called HME) would be suitable for studying the thermal process, since they are likely to be associated with a large overlap between the beam and target nuclei, where there is a greater chance for multiple nucleon-nucleon cascade collisions. In Berkeley

several groups are doing experiments by selecting HME. We show here an example from our data.

We have used 9 sets of tag counter telescopes placed at $\theta = 40°$ to select high multiplicity events. Each telescope selected rather high-energy particles, typically $E_{proton} > 100$ MeV, and it subtended the solid angle of 48 msr. Although the total solid angle covered by 9 counters is small (3.4% of 4π), we can still evaluate with reasonable accuracy the total average multiplicity of charged particles. Collisions studied are Ar + KCl and Ar + Pb at $E_{Beam} = 800$ MeV/A. Our experimental procedure is such that we first selected $M_{Tag} \geqslant 4$ for Ar + KCl and $M_{Tag} \geqslant 5$ for Ar + Pb and then measured light-fragment spectra for such HME using the magnetic spectrometer.

For inclusive events where at least one particle is detected by the spectrometer placed at 40°, the total associated charge-particle multiplicity, m_T, measured by the tag counter was 12 for Ar + KCl and 24 for Ar + Pb. These values are about 30% higher than the average nuclear charge calculated using Eq. (5): $\langle A \rangle = 9$ for Ar + KCl and $\langle Z \rangle = 17$ for Ar + Pb. $m_T > \langle Z \rangle$ partly because m_T includes π^+ and π^- but partly because the detection of one particle by the spectrometer already favors the higher multiplicity.

The participant-spectator model gives a unique relationship between $\langle Z \rangle$ and the maximum impact parameter, b_{max}, as shown in Fig. 12. The total average multiplicity of high-energy particles ($E_p > 100$ MeV) for HME was 25 for $M_{Tag} \geqslant 4$ of Ar + KCl and 49 for $M_{Tag} \geqslant 5$ of Ar + Pb. Values of b_{max} for HME estimated from this model are indicated by arrows in this figure. Because of the selection of high-energy particles by the tag counters, the arrow gives an upper limit of b_{max}.

Fig. 19 shows a comparison of proton spectra between HME and inclusive events for Ar + Pb. For inclusive events we observe both the beam and target fragments in the small p_T region. For HME, however, we observe target fragments only. This is expected with the participant-spectator model. As the impact parameter becomes small, most of the beam nucleus (Ar) becomes the participant, while the target nucleus (Pb) is always partially the participant and partially the spectator at any impact parameter. The suppression of beam fragments further suggests the importance of the multiple nucleon cascade process for HME.

High energy protons in HME show an isotropic angular distribution in the frame whose rapidity is y_0 ($\approx 0.48 \pm 0.03$). As the inclusive events showed forward and backward peaking, this fact again suggests the importance of the multiple nucleon cascade process for HME. If y_0 represents the c.m. frame of the participant piece, the ratio of target charge to beam charge within the participant piece becomes about 1.64, which is larger than the impact-parameter averaged ratio, $\langle Z^{Participant}_{Target} \rangle / \langle Z^{Participant}_{Beam} \rangle = 1.52$, calculated from Eqs. (2) and (3).

In Fig. 20 the proton yields for both inclusive events and HME are plotted as a function of the angle in the frame of $y = y_0$, for three sets of proton energies: 200, 400, and 600 MeV measured in that frame. For Ar + KCl $y_0 = 0.60$ which is close to the nucleon-nucleon c.m. frame. We observe more clearly from this figure than from Fig. 19 that the angular distribution is more isotropic for HME than for inclusive events. For convenience we normalized the HME such that the 90° yield for 600 MeV protons is equal for both inclusive events and HME. Under this normalization we observe the following features:

(1) For HME forward and backward emission is suppressed in Ar + KCl, and the forward emission is especially suppressed in Ar + Pb.

(2) At 90° there is a lower yield of low energy protons for HME in the case of Ar + KCl; namely, low-p_T events are suppressed.

Now let us assume that the proton yield for HME, σ_{HME}, represents the multiple nucleon collision component:

$$\sigma_{HME} \propto \sum_{i=2}^{\infty} \sigma_i \ . \tag{18}$$

Then the inclusive yield, σ, can be written as

$$\sigma = \sigma_1 + \text{const} \cdot \sigma_{HME} \ , \tag{19}$$

Hatch and Koonin[11] calculated the dynamic behavior of σ_1. We use their σ_1 result, except for their normalization. Then we have

$$\sigma = a\,\sigma_{HK} + b\,\sigma_{HME} \ , \tag{20}$$

where σ_{HK} is the calculated result for the CKO process, and a and b are parameters. We searched for the best fit for the observed inclusive data by changing a and b and obtained results giveing very reasonable fits, as shown in Fig. 20. Let us define the ratio P as

$$P = \frac{a\,\sigma_{HK}}{a\,\sigma_{HK} + b\,\sigma_{HME}} \ , \tag{21}$$

Then P shows the fraction due to the CKO component. Using the fitted values of a and b, we estimated the value of P for Ar + KCl over a wide kinematical region of protons. Typical features are:

(1) $P \sim 0$ for high energy protons at 90°. This implies that large-p_T events are mainly from multiple collisions.

(2) The CKO process is dominant for proton production at small angles, even for high-energy protons.

(3) At 90° P $\sim$0.6 for $E_p^* = 200$ MeV. This result is consistent with the data of two particle correlations (Sec. 3.2) where we obtained P $\sim$0.5 for protons with $E_p^* = 182$ MeV at 90°.

The data of associated charge multiplicity give further support to observation (1), as shown in Fig. 21. When we detect small-p_T protons using the spectrometer, the associated charge multiplicity is about 9, while, if we detect large-p_T events, it is 17. This fact confirms that high-p_T protons are mainly from multiple collisions. Furthermore, observation (1) gives the validity of the normalization of the proton data for HME as shown in Fig. 20.

Although the discussion presented here is rather crude and, in particular, the assumption in Eq. (18) has to be more carefully examined, the high-multiplicity events have given further information on the reaction mechanism. In particular, the fraction attributable to the CKO component can be studied over a wide fragment kinematical region by HME, while the two-proton correlation data can give its value in a limited kinematical region.

Finally let us mention a word about the energy spectra for HME. Fig. 22 shows energy distributions of protons and pions. It is expected that the thermal model reproduced them better than the inclusive spectra. So far, the best fit has been obtained by Siemens and Rasmussen in terms of the explosion model. Therefore, the data may suggest an explosion flow from the compressed matter.

3.4 Summary of the Reaction Mechanism

From inclusive data we learned that the nucleus-nucleus collision at relativistic energies has the nature of both the CKO process and the thermal process. Using two-proton correlations and high-multiplicity data we could separate out each process and could determine the fraction due to each process over a wide fragment kinematical region. The current understanding is summarized in Fig. 23.

4. TOPICS

4.1 Reaction Size

In the past few years several theorists[25,26] have suggested a measurement of the Hanbury-Brown/Twiss (H-B/T) effects[27] in heavy-ion collisions. Gyulassy et al.[25,28] further speculated that the peak height of the H-B/T effect is a good measure for studying collective phenomena such as pion condensation.

The H-B/T effect is an interference effect between two particles. If two particles have the same momentum (both magnitude and direction), then there is a strong interference between them. The degree of interference is, however, small if the two particles are located a large distance apart when they are emitted. Similarly, the interference effect disappears when two particles are emitted independently in time.

The first experiment on this effect was done for two π^- fragments by Fung et al.[29] using a streamer chamber. They measured the two-pion correlation function, defined as

$$R \equiv \sigma_0 \frac{d^2\sigma}{d\vec{p}_1 d\vec{p}_2} \Big/ \left(\frac{d\sigma}{d\vec{p}_1}\right)\left(\frac{d\sigma}{d\vec{p}_2}\right)$$
$$= R(\vec{p}_1, \vec{q}) \ , \qquad (22)$$

where $\vec{q}$ is the relative momentum between two pions, $\vec{q} = \vec{p}_1 - \vec{p}_2$. According to Kopylov[30] and Yano and Koonin,[26] this ratio should be given by

$$R = K\left(1 + \frac{2J_1(r_0 q/\sqrt{2})}{1 + (\tau E_0)^2}\right) \qquad \text{(Kopylov)}$$

$$\simeq K\left[1 + \exp(-\tau^2 E_0^2/2)\exp(-r_0^2 q^2/2)\right] \quad \text{(Yano-Koonin)}\ , \qquad (23)$$

where τ and r_0 are the reaction time and the reaction size. The data give $\tau \sim 5 \times 10^{-24}$ and r_0(overall) $\simeq (3.3 \pm 0.9)$ fm for 1.8 GeV/A Ar + Pb_3O_4. Typical examples of the data are shown in Fig. 24. For high multiplicity events an even larger value of r_0 was observed. According to the participant-spectator model, the average radius $\langle r_0 \rangle$ for Ar + Pb becomes $\langle r_0 \rangle \sim 4.2$ fm for the normal density participant. This value is comparable to the observed one.

When the two emitted particles are a proton and a neutron, we expect an interference effect in the inclusive deuteron spectrum. Mekjian[13] developed the theory of complex particle formation in terms of the thermal model and demonstrated that the reaction size can be derived from proton and deuteron spectra. According to the phase-space argument, the probability of producing a deuteron at a velocity $\vec{v}_d$ is proportional to the probability of finding a proton and a neutron with the same velocity, namely

$$P_d(\vec{v} = \vec{v}_d) \propto P_p(\vec{v} = \vec{v}_d) \cdot P_n(\vec{v} = \vec{v}_d)\ , \qquad (24)$$

where $P(\vec{v})$ is the probability of a particle having velocity $\vec{v}$. This is the well-known idea of coalescence,[31] sometimes called the final state interaction. In relativistic collisions the spectra of neutrons are approximately replaced by those of protons. Therefore we have

$$\sigma_d(E = E_d) = A\,[\sigma_p(E = E_d/2)]^2, \tag{25}$$

where A is a constant. Fig. 25 shows that prediction (25) works well over a wide kinematical region. The coefficient A is almost independent of the beam energy but depends on the mass of beam and target nuclei, as can be seen from Fig. 26. This fact tells us that the complex-fragment emission reflects the geometrical aspect and the dynamics of the final state interactions but not the formation or dynamics of the primary protons and neutrons.

We can guess that $A \propto f_1 f_2$ where f_1 includes the dynamics of formation of a complex fragment, such as the radius of the complex fragment or the interaction strength between proton and neutron, and f_2 includes the reaction size and reaction time of heavy-ion collisions Unfortunately we do not have a complete formula in this respect, but in Fig. 27 we show the quantity r_0 deduced from the formula of Mekjian which is proportional to $(f_1 f_2)^{-1/3}$. This quantity r_0 represents the reaction size but still includes the effect of f_1, the dynamics. This point is open to future studies.

4.2 90° Peak of Low-Energy π^+

Detection of low-energy pions is an interesting project, as some theorists have proposed that, if a phase transition such as pion condensation or quark matter exists, it may be sensitively reflected in low-energy pion production.

Chiba et al.[32] and Wolf et al.[33] have recently observed that low-energy positive pions are enhanced at c.m. 90° at a certain $p_T (p_T \sim 0.5\ m_\pi c)$ for equal-mass collisions such as Ne + NaF and Ar + Ca at beam energies around 0.8-1 GeV/A. This 90° peaking is independent of the fragment multiplicity.

The results are shown in Figs. 28 and 29 where the data are compared with the $p + p \to \pi^+$ data. The 90° peaking is a phenomenon specific to heavy-ion collisions. Explanation of this peak is not yet available, but there are several suggestions, such as its being due to the Coulomb effect,[34] the blast wave,[19] or two Δ-sources in projectile and target. It encourages further measurements of both π^+ and π^- using a magnetic spectrometer.

4.3 Backward Particle Production

Measurements of backward-emitted particles are ideal for studying nuclear collectivity, since, if the nucleus behaves just like an assembly of nucleons without any mutual correlations, then the backward production is not kinematically allowed, unless the Fermi motion of nucleons is exceptionally large.

A Russian group[35] first started the backward production measurements and proposed the cumulative model where a sort of cluster (fluctuon) due to a strong nucleon-nucleon correlation inside the nucleus is assumed. Nucleus production at backward angles could be explained, according to them, by the scattering of the nucleon by such a cluster. Frankel[15] later proposed an alternative explanation of their data for backward production, namely the existence of very large Fermi motion of the form of

$$\Sigma p_i \propto \exp(-p/p_0) \ , \tag{26}$$

with $p_0 \sim 90$ MeV/c.

The idea of the cluster may be closely related to the idea of a large effective Fermi motion, since the origin of the cluster is a short-range correlation among the nucleons and its Fourier transform gives a long tail in momentum space.

Recently Schroeder et al.[36] observed the beam energy dependence of p_0 in Eq. (26), as shown in Fig. 30. (In the figure it is named k_0.) If nucleons inside the nucleus have an intrinsic Fermi motion distribution given by Eq. (26), then the value p_0 should not depend on the beam energy. The data clearly show the beam-energy dependence. Therefore, it is more appropriate to think that the parameter p_0 effectively includes several collision effects such as the cluster collision and multiple collisions. We note that the assumption of Eq. (9) mentioned in Sec. 3.1 is based on Eq. (26).

4.4 Total Energy Dependence of Charged-Particle Multiplicity

Recently Poskanzer et al.[37] found an interesting result, shown in Fig. 31, which cannot be understood in terms of the available theoretical tools. They find that the total charged-particle multiplicity observed in several different beams on a uranium target depends on the total available beam energy only. In Sec. 2 we showed that energy/nucleon determines the collision dynamics. The present data show that total energy determines the observed quantity. This is a very interesting observation, but it is hard to explain it.

4.5 Forward Suppression at High Multiplicity

In Sec. 3.3 we showed that the particle emission at forward angles is suppressed for high-multiplicity events compared to the inclusive data. The reason was very simple; namely the projectile fragment is missing in high-multiplicity events.

Gutbrod et al.[38] recently showed that, when high multiplicity events were selected, the yield of protons at 20° (lab) became less than that at 30° (lab). Their preliminary data are shown in Fig. 32.

If this observation is correct, then the data suggest several things. It may be simply due to the fact that it is easier for the beam particle to escape sideways rather than to penetrate the thick nucleus lying in the forward direction. It may represent the positive evidence of a hydrodynamical flow that was suggested by Nix et al.[39] Or perhaps it may indicate the presence of a Mach cone, as was previously suggested by emulsion work.[40] We cannot judge at the present stage what types of physics are hiding behind this observation, $I(30°) < I(20°)$ at high multiplicity.

5. SUMMARY AND RELATION TO LOW-ENERGY PHYSICS

In Secs. 2 and 3 we learned that the geometry of collisions is well described in terms of the participant-spectator model and that the dynamics of the participant piece is described as a superposition of single knock-out and multiple nucleon-nucleon scatterings. The idea of the participant-spectator model is meaningful when the de Broglie wave length of the incident beam nucleons is small compared to the distance between nucleons inside the nucleus. This means that the model can be applied when

$$\lambda_d = \frac{\hbar}{p} << d \simeq 1.8 \text{ fm} , \tag{27}$$

where d is the internucleon distance. The above relation is satisfied when the beam energy in the c.m. frame is more than 10-20 MeV/A. Below a c.m. energy of 5 MeV/A the individuality of each nucleon disappears and both participant and spectator are combined to form the well-known compound nucleus. The study of this model with beam energies of 10-100 MeV/A is thus very interesting.

Although the thermal model does not describe the whole area of

collision dynamics, it is worthwhile to study how well the model can describe the collision dynamics at lower energies. We plot the temperature calculated by Eq. (7) by a dotted curve on the famous diagram created by Scott[41] in Fig. 33. From the momentum distribution of projectile fragments[5] it has been known, although we have not discussed it in the present paper, that the beam spectator can be heated up to a limiting temperature of 8 MeV/A.[42] Such a temperature is also plotted in the figure. The temperature of the participant intersects with that of the spectator at the c.m. beam energy of 12 MeV/A. Above 10-20 MeV/A, therefore, the two temperature components start to separate out. It is thus again interesting to study the collision dynamics with beam energies from 10-100 MeV/A.

In the present paper we have not discussed angular momentum, because no theories treat it correctly. Although it is expected that the angular momenta carried by the spectator and participant are not large at high energies, it is worthwhile to test this. As illustrated in Fig. 34, we can imagine several methods for this purpose. For beam fragments we can easily identify the product nucleus by the dE/dx - E method. If the product nucleus is β-unstable, its polarization can be detected from measurements of β-decay asymmetry. For target fragments the measurements of isomer ratio and γ-multiplicity would be powerful. We have no clean methods to measure the angular momentum of the participant piece, but it is possible to determine it by detecting particle correlations at large angles.

It has been shown that the complex-fragment emission can be explained by means of the coalescence model which depends on the reaction size. We know that the coalescence radius, p_0, is almost independent of the beam energy in the region of 400 MeV < E_{Lab} < 2.1 GeV per nucleon. However, its study at lower energies may have to be done.

The importance of the single CKO process has been studied in Sec. 3.2. The thermal model becomes more adequate to describe the collisions at lower beam energies, as the total cross section of nucleon-nucleon scatterings becomes larger at lower energies. The fraction of the CKO component as a function of the beam energy is thus an interesting quantity.

As a whole, there is a large gap in the interpretation of physics at high energy and that at low energy. However, most of the aspects are common down to a fairly low energy, and it is certainly worthwhile and interesting to test several concepts which have emerged from relativistic heavy-ion studies at lower beam energies.

6. ACKNOWLEDGMENTS

Most of the data described here have been obtained in collaboration with O. Chamberlain, M.-C. Lemaire, S. Schnetzer, G. Shapiro, H. Steiner, and I. Tanihata (see Refs. 44-48). The author would like to express his sincere thanks to all of them. The help by L. Anderson and W. Brückner at the early stage of the experiment is also gratefully acknowledged. Thanks are also due to A. M. Poskanzer and L. S. Schroeder for their permission to show their data prior to publication. Calculations of the clean knock-out process by R. L. Hatch and S. E. Koonin for the purpose of this manuscript are also acknowledged. This work is supported by the Nuclear Science Division of the U.S. Department of Energy, under Contract W-7405-ENG-48, and by the Yamada Foundation.

REFERENCES

1. Part of the talks are compiled in Proc. 2nd High-Energy Heavy-Ion Summer Study, Berkeley, 1972, LBL03675.
2. Refer to the talks given by W. Benenson, T. J. M. Symons and K. Van Bibber in this Conference.
3. L. Anderson, Ph.D. Thesis, LBL-6767 (1977).
4. P. J. Lindstrom, D. E. Greiner, H. H. Heckman, B. Cork, and F. S. Bieser, LBL-3650 (1975), unpublished.
5. D. E. Greiner, P. J. Lindstrom, H. H. Heckman, B. Cork, and F. S. Bieser, Phys. Rev. Lett. 35, 152 (1975); H. H. Heckman, D. E. Greiner, P. J. Lindstrom and H. Shwe, Phys. Rev. C17, 1735 (1978); G. D. Westfall, L. D. Wilson, P. J. Lindstrom, H. J. Crawford, D. E. Greiner, and H. H. Heckman, Phys. Rev. C19, 1309 (1978).
6. J. Papp, Ph.D. Thesis, LBL-3633 (1975).
7. J. Hüfner, Proc. 4th High Energy Heavy Ion Summer Study, Berkeley, 1978, LBL-7766, p. 135; J. Hufner and J. Knoll, Nucl. Phys. A290, 460 (1977).
8. D. J. Morrisey, W. Loveland, M. de Saint Simon and G. T. Seaborg, LBL-8983 (1979).
9. S. E. Koonin, Phys. Rev. Lett. 39, 680 (1977).
10. I. A. Schmidt and R. Blankenbecler, Phys. Rev. D15, 3321 (1977).
11. R. L. Hatch and S. E. Koonin, Phys. Lett. 81B, 1 (1978).
12. G. D. Westfall, J. Gosset, P. J. Johansen, A. M. Poskanzer, W. G. Meyer, H. H. Gutbrod, A. Sandoval, and R. Stock, Phys. Rev. Lett. 37, 1201 (1976); J. Gosset, H. H. Gutbrod, W. G. Meyer, A. M. Poskanzer, A. Sandoval, R. Stock, and G. D. Westfall, Phys. Rev. C16, 629 (1977).

13. A. Z. Mekjian, Nucl. Phys. A312, 491 (1978); Phys. Rev. C17, 1051 (1978); Phys. Rev. Lett. 38, 604 (1977).

14. M. Sobel, P. J. Siemens, J. P. Bondorf and H. A. Bethe, Nucl. Phys. A251, 502 (1975).

15. S. Frankel, Phys. Rev. Lett. 38, 1338 (1977).

16. J. Gosset, J. I. Kapusta and G. D. Westfall, Phys. Rev. C18, 844 (1978).

17. J. I. Kapusta, Phys. Rev. C16, 1493 (1977).

18. M. Sano, private communication, 1979.

19. P. J. Siemens and J. O. Rasmussen, Phys. Rev. Lett. 42, 880 (1979).

20. T. P. Clements and L. Winsberg, UCRL-9043 (1960), unpublished.

21. W. Myers, Nucl. Phys. A296, 177 (1978).

22. S. Das Gupta, Phys. Rev. Lett. 41, 1450 (1978).

23. R. K. Smith and M. Danos, private communication, 1978.

24. Y. Yariv and Z. Fraenkel, preprint, 1979.

25. M. Gyulassy, LBL-7704 (1978).

26. F. B. Yano and S. E. Koonin, Phys. Lett. 78B, 556 (1978).

27. R. Hanbury-Brown and R. Q. Twiss, Nature 178, 1046 (1956).

28. M. Gyulassy, S. K. Kauffman, and L. W. Wilson, LBL-8759 (1979).

29. S. Y. Fung, W. Gorn, G. P. Kiernan, J. J. Lu, Y. T. Oh and R. T. Poe, Phys. Rev. Letters 41, 1592 (1978).

30. G. I. Kopylov, Phys. Lett. 50B, 472 (1974).

31. H. H. Gutbrod, A. Sandoval, P. J. Johansen, A. M. Poskanzer, J. Gosset, W. G. Meyer, G. D. Westfall and R. Stock, Phys. Rev. Lett. 37, 667 (1976); S. F. Butler and C. A. Pearson, Phys. Rev. 129, 836 (1963).

32. J. Chiba, K. Nakai, I. Tanihata, S. Nagamiya, H. Bowman, J. Ingersoll, and J. O. Rasmussen, LBL-8699 (1979).

33. K. L. Wolf, H. H. Gutbrod, W. G. Meyer, A. M. Poskanzer, A. Sandoval, R. Stock, J. Gosset, C. H. King, G. King, N. Van Sen and G. D. Westfall, Phys. Rev. Lett. 42, 1448 (1979).

34. S. E. Koonin, seminar talk at LBL, 1979.

35. A. M. Baldin, AIP Conference Proceedings 26, 620 (1975); V. V. Burov, V. K. Lukyanov and A. I. Titov, Phys. Lett. 67B, 46 (1977).

36. L. S. Schroeder et al., private communication, 1979.

37. A. M. Poskanzer et al., private communication, 1979.

38. H. H. Gutbrod, Proc. 4th High Energy Heavy Ion Summer Study, Berkeley, 1978, LBL-7766, p. 1.

39. A. A. Amsden, F. H. Harlow and J. R. Nix, Phys. Rev. C15, 2059 (1977).

40. H. G. Baumgardt, J. V. Schott, Y. Sakamoto, E. Schopper, H. Stocker, J. Hofman, W. Scheid and W. Greiner, Z. Physik A273, 359 (1975).

41. D. K. Scott, private communication, 1979.

42. A. S. Goldhaber, Phys. Lett. 53B, 306 (1974).

43. K. Sugimoto, A. Mizobuchi, K. Nakai, and K. Matsuda, Phys. Lett. 18, 38 (1965).

44. S. Nagamiya, I. Tanihata, S. Schnetzer, L. Anderson, W. Brückner, O. Chamberlain, G. Shapiro, and H. Steiner, J. Phys. Soc. Japan 44 Suppl. 378 (1978).

45. S. Nagamiya, Proc. 4th High Energy Heavy Ion Summer Study, Berkeley, 1978, LBL-7766, p. 71.

46. S. Nagamiya, L. Anderson, W. Brückner, O. Chamberlain, M.-C. Lemaire, S. Schnetzer, G. Shapiro, H. STeiner, and I. Tanihata, Phys. Lett. 81B, 147 (1979).

47. M.-C. Lemaire, S. Nagamiya, S. Schnetzer, H. Steiner, and I. Tanihata, Phys. Lett. (in press).

48. I. Tanihata, S. Nagamiya, O. Chamberlain, M.-C. Lemaire, S. Schnetzer, G. Shapiro, and H. Steiner, LBL-9352 (1979).

FIGURE CAPTIONS

Fig. 1. Fragment spectra at 0° in collisions of 2.1 GeV/A α+ C plotted as a function of lab. momentum (left) and as a function of rapidity (right). y_B indicates the beam rapidity.

Fig. 2. Proton spectra at large angles in collisions of 800 MeV/A Ar + KCl. p_{Beam}/A indicates the beam momentum per nucleon.

Fig. 3. Participant-spectator model. After the collision non-overlapped parts of the beam and target nuclei form the beam spectator and target spectator, while the overlapped part forms the participant piece. In the plane of $p^*_{\parallel}/mc$ and p_T/mc the beam and target spectators are sharply peaked at p^*_{Beam}/A and p^*_{Target}/A, respectively, while the participant emits particles at all angles.

Fig. 4. Total yield of nuclear charges emitted at 0° as compared with the prediction by Eq. (4).

Fig. 5. Total yield of nuclear charges emitted at large angles ($0° < \theta < 180°$) as compared with the prediction by Eq. (5). Data at $10° < \theta < 145°$ were used and extrapolated to 0° and 180°.

Fig. 6. Proton spectra at $\theta_{c.m.} = 90°$ in collisions of C + C, Ne + NaF, and Ar + KCl at $E_{Beam} = 800$ MeV/A. T = 82 MeV was used for the thermal model (see text).

Fig. 7. Proton and pion spectra at $\theta_{c.m.} = 90°$ in collisions of 800 MeV/A Ne + NaF.

Fig. 8. Beam-energy dependence of proton spectra at $\theta_{c.m.} = 90°$ in collisions of Ne + NaF.

Fig. 9. Plot of exponential slope factor, E_0, of proton and pion spectra at c.m. 90° for collisions of Ne + NaF as a function of c.m. beam energy. Solid curve was calculated from Eq. (7) with $\rho_0/\rho = 1$,

and dotted curve was calculated with our Monte-Carlo code. The latter can be applied to proton slope only.

Fig. 10. $d\sigma/d\Omega$ at c.m. 90° for protons and pions in collisions of Ne + NaF, plotted as a function of the c.m. beam energy per nucleon. Solid curves were calculated from Eq. (1) with $\rho_0/\rho = 1$ and dotted curves from Eq. (12). Both curves were normalized to the data at the point of proton yield for 400 MeV/A.

Fig. 11. Angular distribution of protons in the c.m. frame in 800 MeV/A Ar + KCl, as compared with the thermal and clean-knock-out models.

Fig. 12. Experimental layout of the two-proton correlation measurements. θ_R, θ_U and θ_D were fixed at 40° and θ_{sp} was varied.

Fig. 13. Contour plot of the degree of coplanarity defined by Eq. (13) for C + C and Ar + KCl at E_{Beam} = 800 MeV/A. Dotted circle indicates the kinematics of p-p elastic scattering when the internal motion of protons inside the nucleus is ignored. Cross-hatched area indicates the kinematical region covered by the R-telescope shown in Fig. 12.

Fig. 14. Fit of the degree of coplanarity, C, using an exponential-type momentum distribution, $\exp(-p/p_0)$ with $\langle p \rangle$ = 260 MeV/c.

Fig. 15. Effect of particle multiplicity on the value of the degree of coplanarity, C, in the extreme case where the nucleus-nucleus collision is the superposition of pure nucleon-nucleon elastic scatterings only. The value of (C - 1) becomes proportional to $1/m_T$ when a sufficiently large number of nucleons are involved in the collision.

Fig. 16. Values of C-1 at the peak in the contour map of C (see Fig. 13) plotted as a function of the total charged-particle multiplicity m_T.

Theoretical curves are labeled according to the percentage of single clean-knock-out contribution to total yield; P is defined by Eq. (15). Cross-hatched areas indicate experimental points obtained in C + C, Ne + NaF and Ar + KCl at E_{Beam} = 800 MeV/A.

Fig. 17. Degree of coplanarity in collisions of C + Pb at 800 MeV/A. The ratio C is smaller than 1 and this observation suggests the existence of nuclear shadowing, as illustrated in the lower part.

Fig. 18. Average nuclear charge $\langle Z \rangle$ for the participant piece plotted as a function of the maximum impact parameter of the collision. Solid curves are predictions of the participant-spectator model. Impact-parameter bias by our tag counters is indicated by an arrow. Since relatively high-energy protons (E_p > 100 MeV) were selected by the tag counters, the arrow gives an upper limit of the maximum impact parameter.

Fig. 19. Proton spectra in 800 MeV/A Ar + Pb for inclusive (above) and high-multiplicity (below) events.

Fig. 20. Proton angular distributions for inclusive and high-multiplicity events plotted as a function of the angle in the c.m. frame of the participant piece in collisions of Ar + KCl and Ar + Pb at E_{Beam} = 800 MeV/A. Theoretical values for the clean-knock-out component are shown by dotted curves. Sums of clean-knock-out component and the high-multiplicity events, defined by Eq. (20), are indicated by solid curves which can be compared with the inclusive data.

Fig. 21. Associated charged-particle multiplicity distribution when one proton is detected in the mid-rapidity region at low p_T (black circle) and at high p_T (open circle). A larger number of total associated

multiplicity is observed when a high-p_T proton is detected.

Fig. 22. Energy spectra of protons and pions for high multiplicity events in 800 MeV/A Ar + KCl.

Fig. 23. Current understanding of the reaction mechanism of heavy-ion collisions studied from the proton production. It is illustrated in the plane of $p_{\parallel}^{*}/mc$ and p_T/mc for proton fragments.

Fig. 24. The ratio R defined by Eq. (22) as a function of the relative pion momentum $|\vec{q}|$. 1.8 GeV/nucleon ^{40}Ar beam incident on (a) BaI_2 and (b) Pb_3O_4 in an "inelastic" triggering mode, and on (c) Pb_3O_4 triggering on the most central collisions, where "inelastic" means 10-15% of peripheral inelastic scatterings are included. Data are taken from Ref. 29.

Fig. 25. Deuteron spectra compared with the prediction of the coalescence model in collisions of 800 MeV/A Ar + KCl. Open squares and diamonds are calculated by squaring the proton spectra.

Fig. 26. Coalescence radius, p_0, for deuteron/(proton)^2 as a function of the beam energy for Ne + NaF and Ne + Pb.

Fig. 27. Radius R evaluated from the data of complex fragments and by using the thermal model formula by Mekjian,[13] plotted vs $(A_B^{1/3} + A_T^{1/3})$. Data for beams at 800 MeV/A are used. Empirical fits of R in terms of $(A_B^{1/3} + A_T^{1/3})$ are given in the figure.

Fig. 28. Contour plot of invariant cross sections of positive pions produced in 800 MeV/A Ne + NaF (left) and 730 MeV/A p + p (right), taken from Ref. 32.

Fig. 29. Contour plot of invariant cross sections of positive pions produced in 1.05 GeV/A Ar + Ca (above) and 730 MeV/A p + p (below), taken from Ref. 33.

Fig. 30. Exponential slope of the proton momentum distribution inside the nucleus, p_0, defined by Eq. (26) as a function of the beam energy. In this figure p_0 is named k_0. Values were calculated from the data on backward production in collisions of p + Cu by Schroder et al.[36]

Fig. 31. Charged-particle multiplicity distribution associated with one proton (E_p = 40 - 200 MeV) detected at θ_{Lab} = 90°, plotted as a function of total energy of the beam with uranium target. Data are taken from Ref. 37.

Fig. 32. Proton yields for high-multiplicity events in collisions of 400 MeV/A Ne + U. Data are taken from Ref. 38.

Fig. 33. Nuclear temperature vs. beam energy plotted by Scott.[41] The temperature for the participant and for the spectator are superposed on it. The two temperatures become equal at ($E_{c.m.}$ - V)/nucleon = 12 MeV.

Fig. 34. Participant and spectator model with angular-momentum effect taken into consideration. Possible methods to measure angular momenta are indicated.

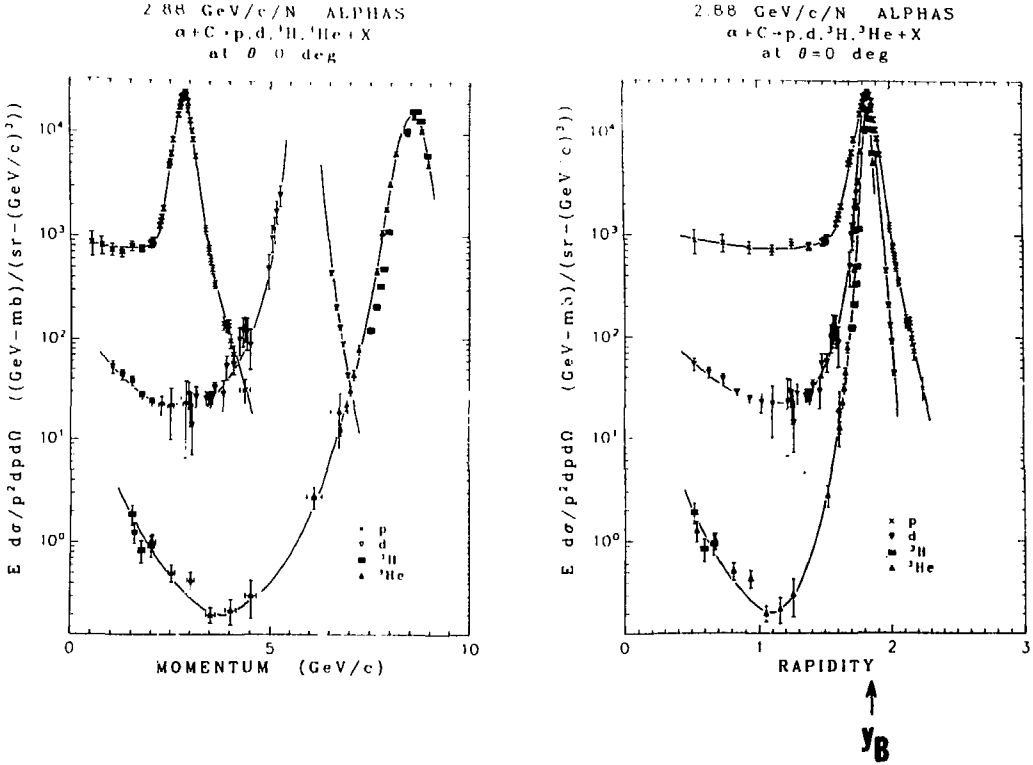
2.88 GeV/c/N ALPHAS
α+C→p,d,³H,³He+X
at θ=0 deg
E dσ/p²dpdΩ ((GeV-mb)/(sr-(GeV/c)²))
MOMENTUM (GeV/c)
p
d
³H
³He
2.88 GeV/c/N ALPHAS
α+C→p,d,³H,³He+X
at θ=0 deg
E dσ/p²dpdΩ (GeV-mb)/(sr-(GeV/c)²))
RAPIDITY
p
d
³H
³He
y_B

Fig. 1

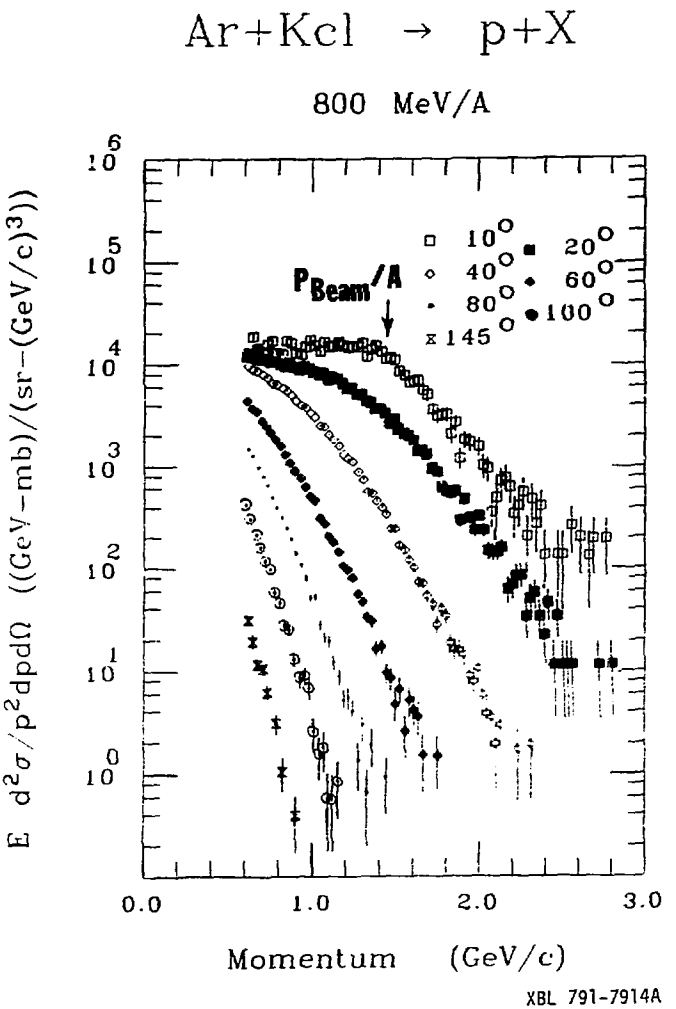
Ar+Kcl → p+X
800 MeV/A
P_{Beam}/A
10°
20°
40°
60°
80°
100°
145°
$E\ d^2\sigma/p^2dpd\Omega$ ((GeV-mb)/(sr-(GeV/c)^3))
10^6
10^5
10^4
10^3
10^2
10^1
10^0
0.0
1.0
2.0
3.0
Momentum (GeV/c)
XBL 791-7914A

Fig. 2

Participant-Spectator Model

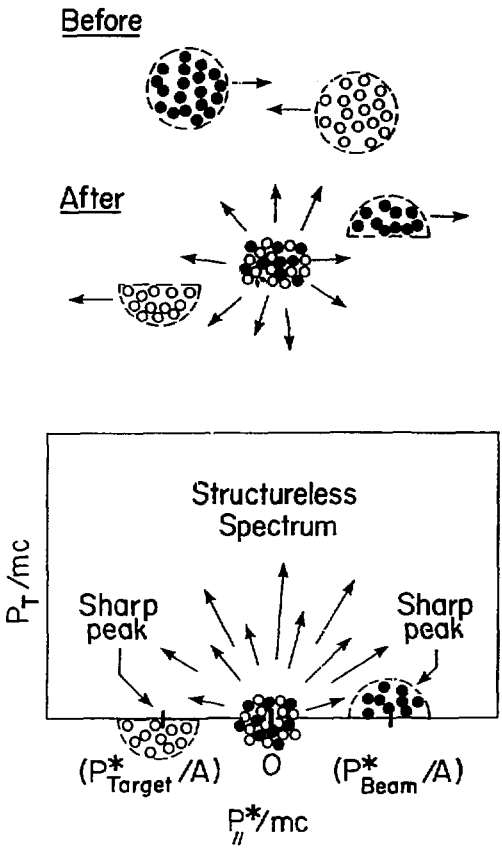

XBL 797 - 2087

Fig. 3

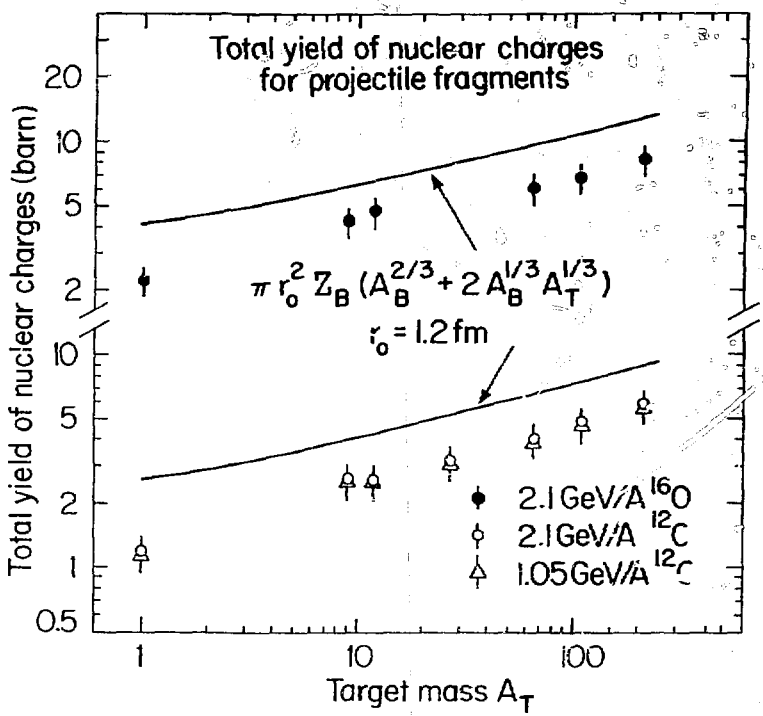

XBL 797 - 2083

Fig. 4

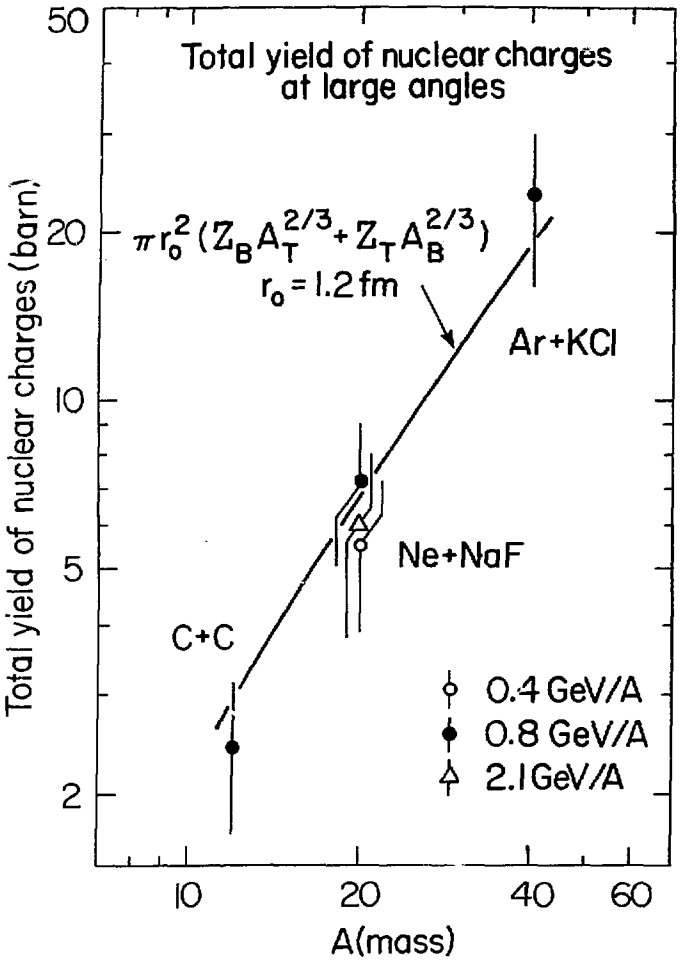

XBL 797 - 2084

Fig. 5

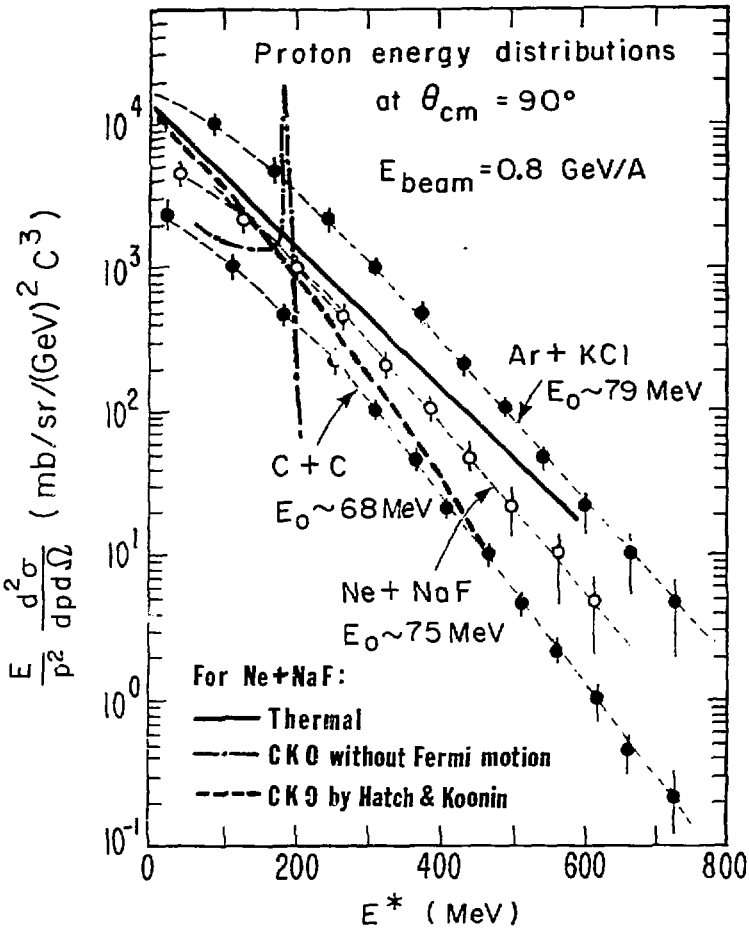
Proton energy distributions
at θ_{cm} = 90°
E_{beam} = 0.8 GeV/A
Ar + KCl
E_0~79 MeV
C + C
E_0~68 MeV
Ne + NaF
E_0~75 MeV
For Ne+NaF:
Thermal
CKO without Fermi motion
CKO by Hatch & Koonin
$E \frac{d^2\sigma}{dp\,d\Omega}$ (mb/sr/(GeV)^2 c^3)
10^4
10^3
10^2
10^1
10^0
10^{-1}
0
200
400
600
800
E^* (MeV)

Fig. 6

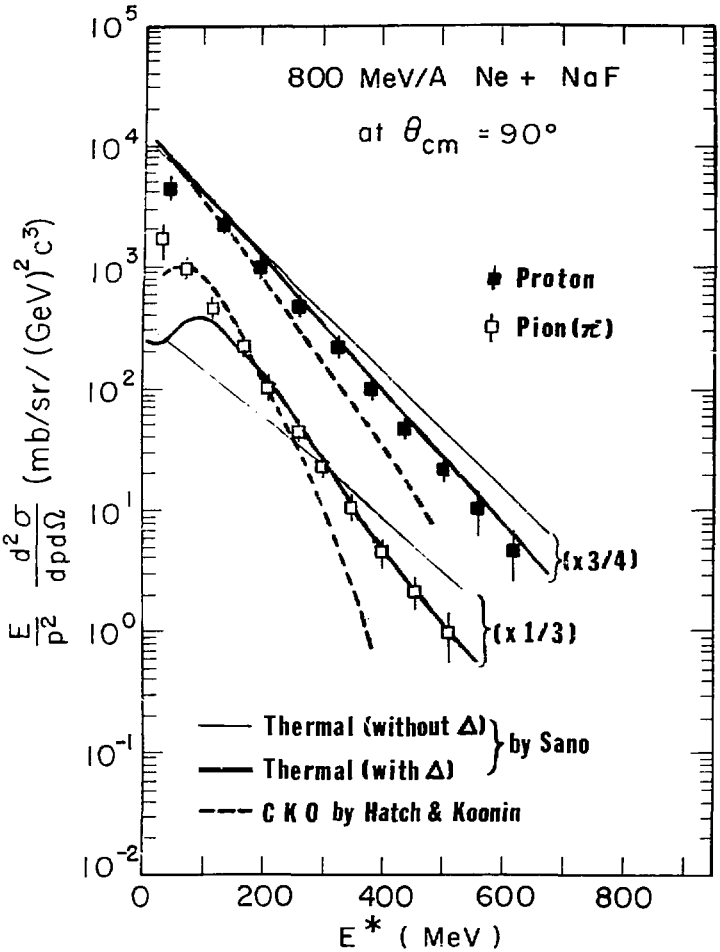

XBL 788-1581A

Fig. 7

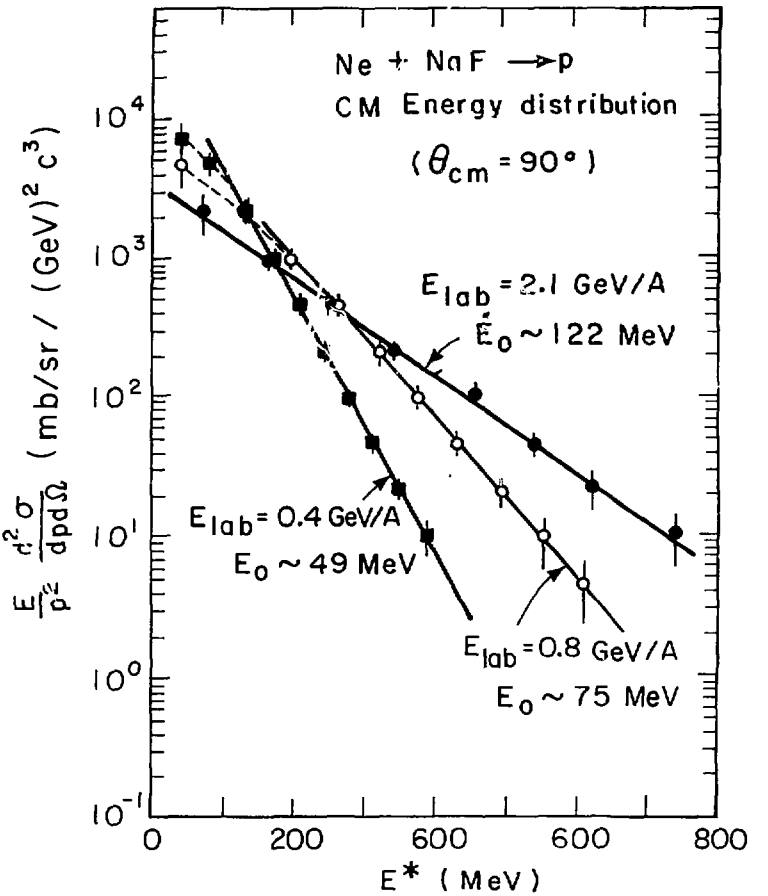

XBL 788-1493

Fig. 8

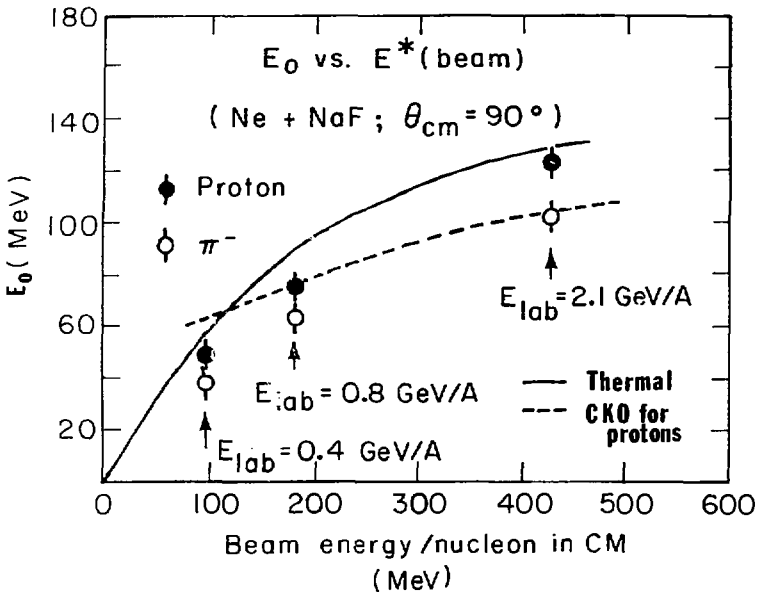

XBL 788-1495A

Fig. 9

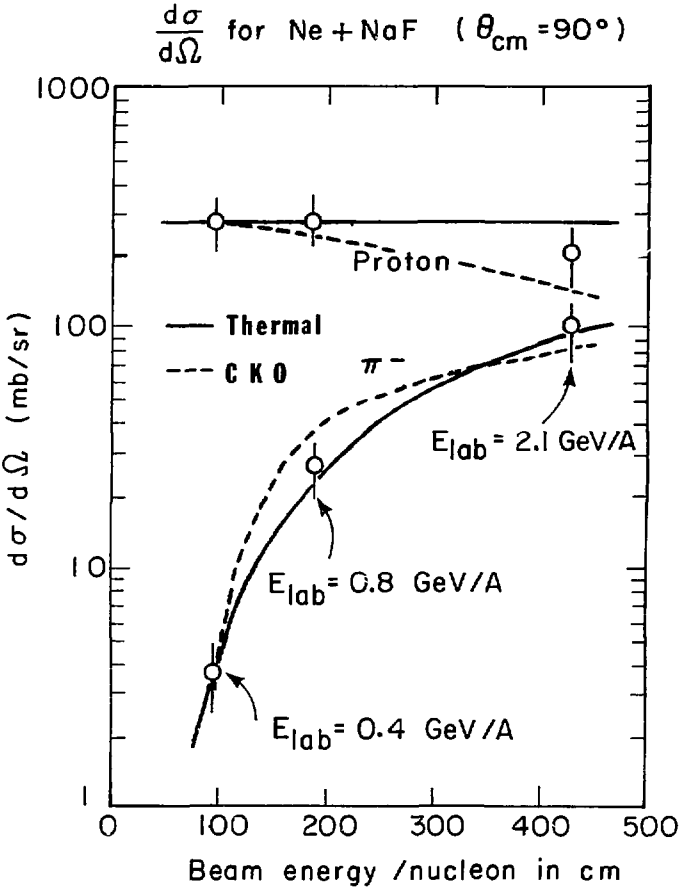

XBL 788-1496A

Fig. 10

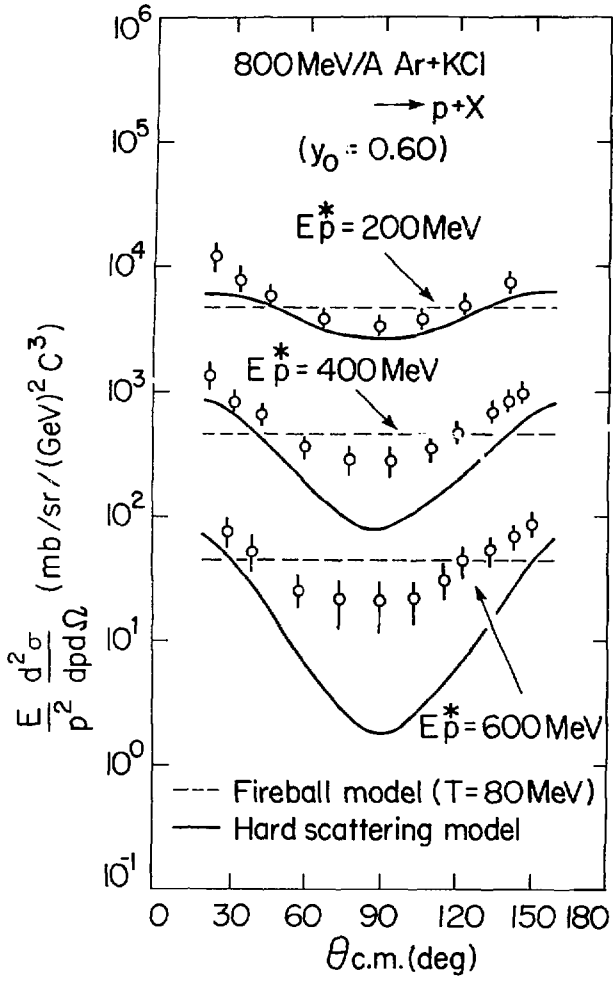

XBL 797 - 2085

Fig. 11

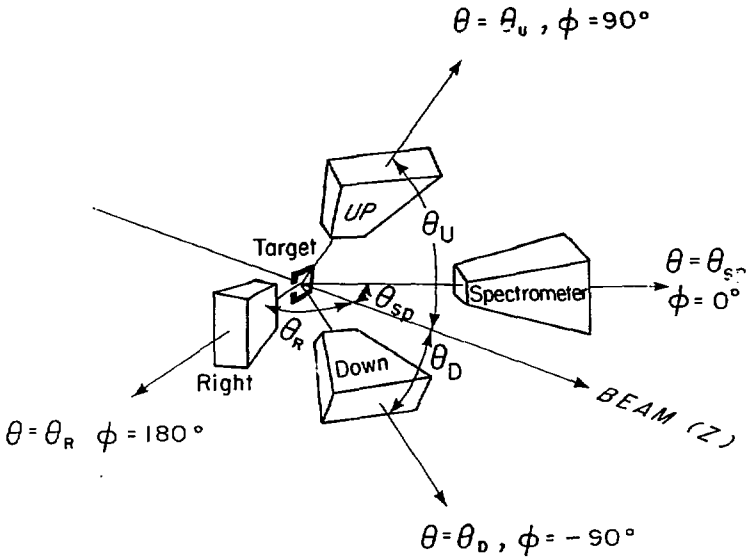
θ = θU , φ = 90°
UP
θU
Target
θ = θSp
φ = 0°
Spectrometer
θSp
θR
Right
Down
θD
BEAM (Z)
θ = θR φ = 180°
θ = θD , φ = − 90°

Fig. 12

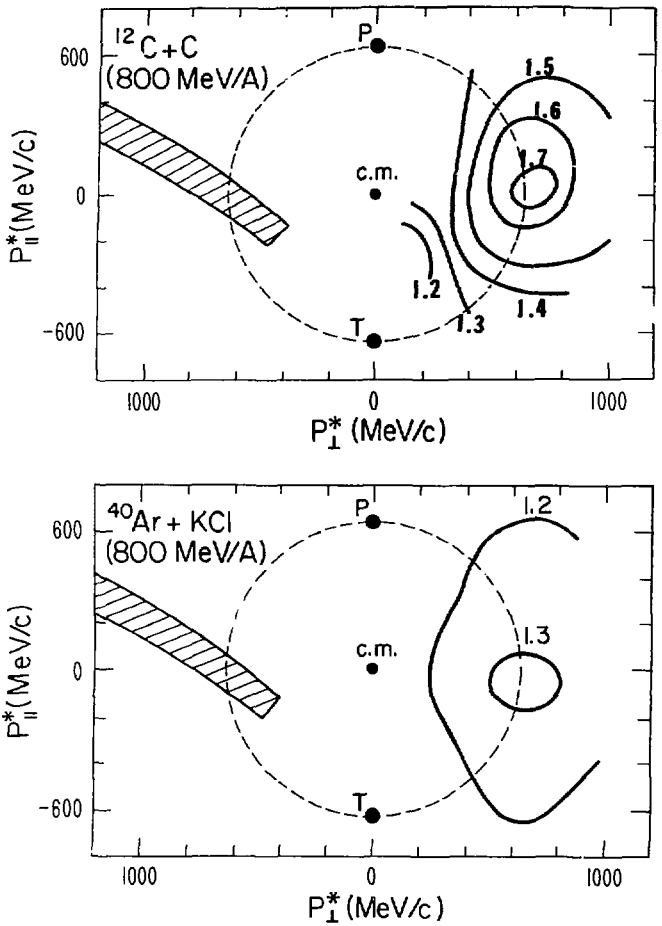

XBL 793-761A

Fig. 13

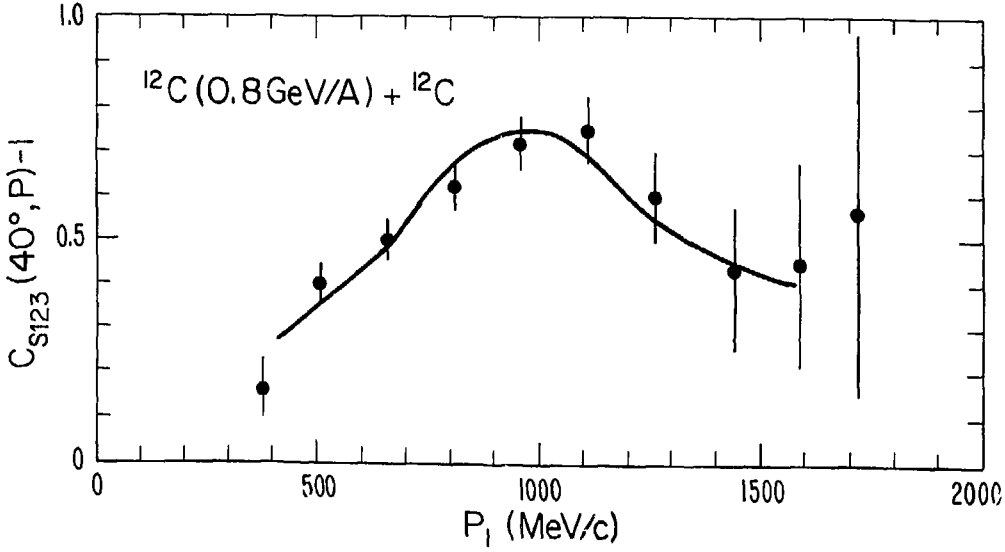

XBL 793-765

Fig. 14

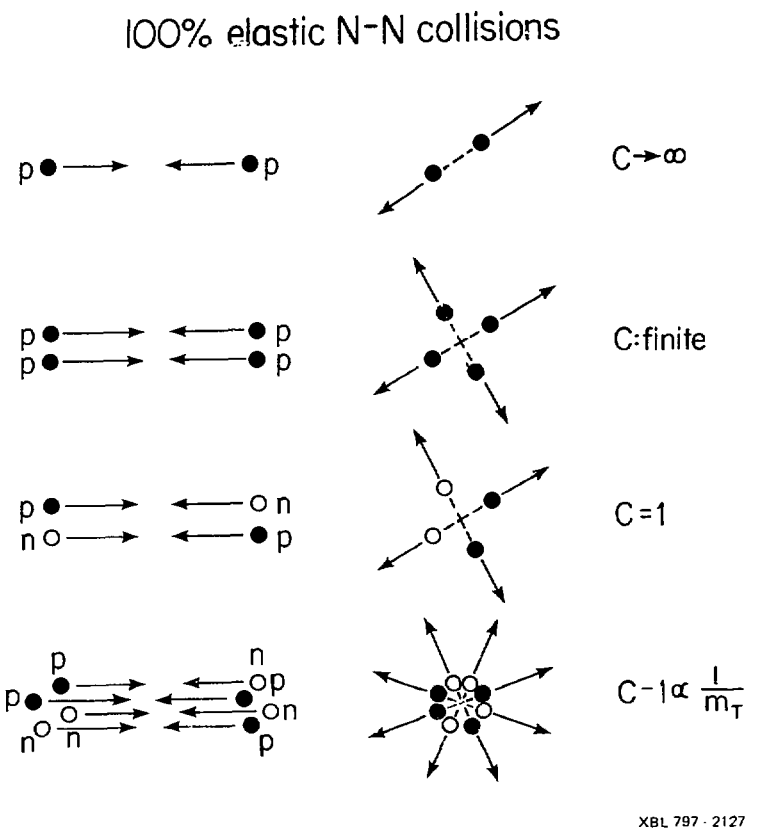

Fig. 15

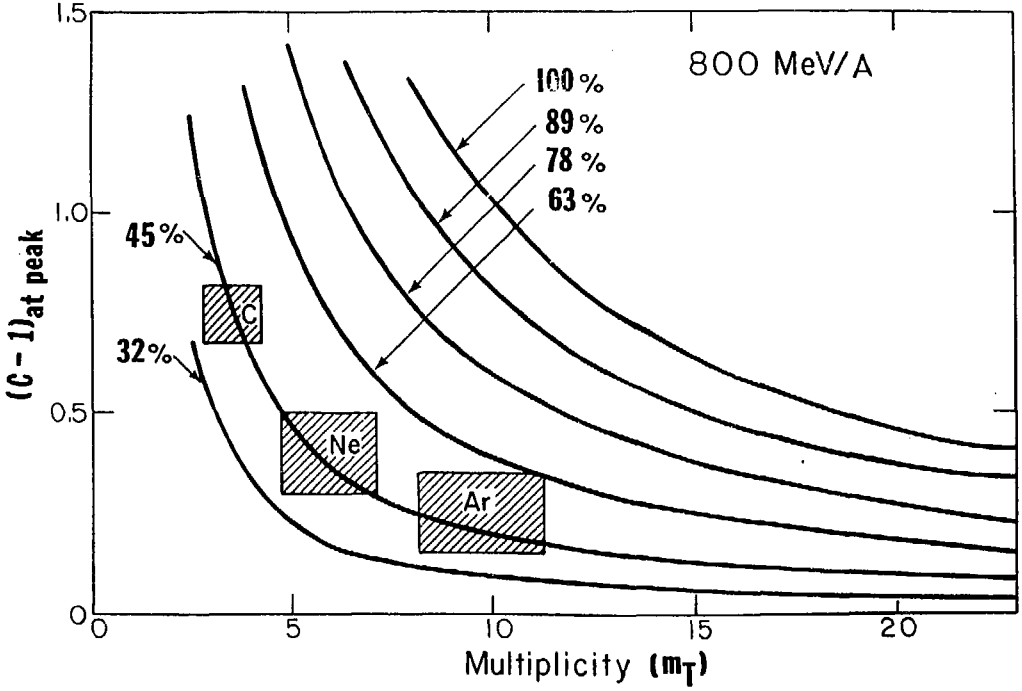
800 MeV/A
100 %
89 %
78 %
63 %
45 %
32 %
C
Ne
Ar
1.5
1.0
0.5
0
0
5
10
15
20
(C − 1)at peak
Multiplicity (mT)

Fig. 16

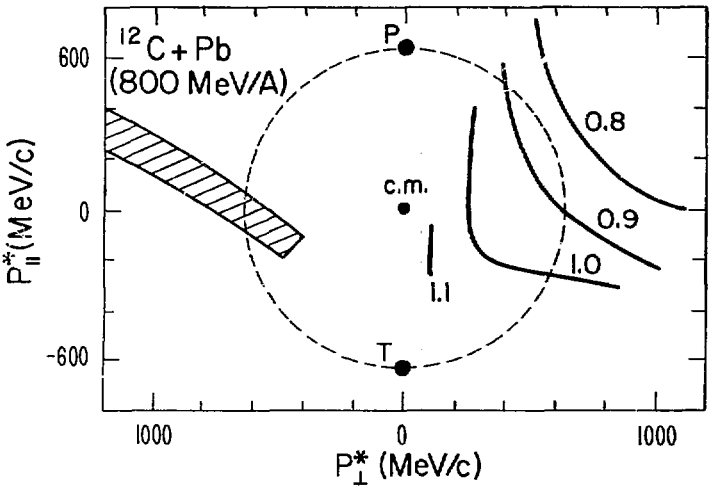

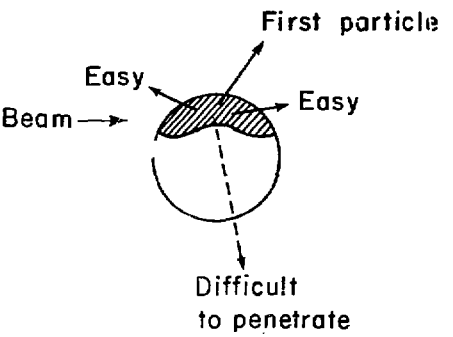

Shadowing observed in
two-particle correlation

XBL 7812-13627A

Fig. 17

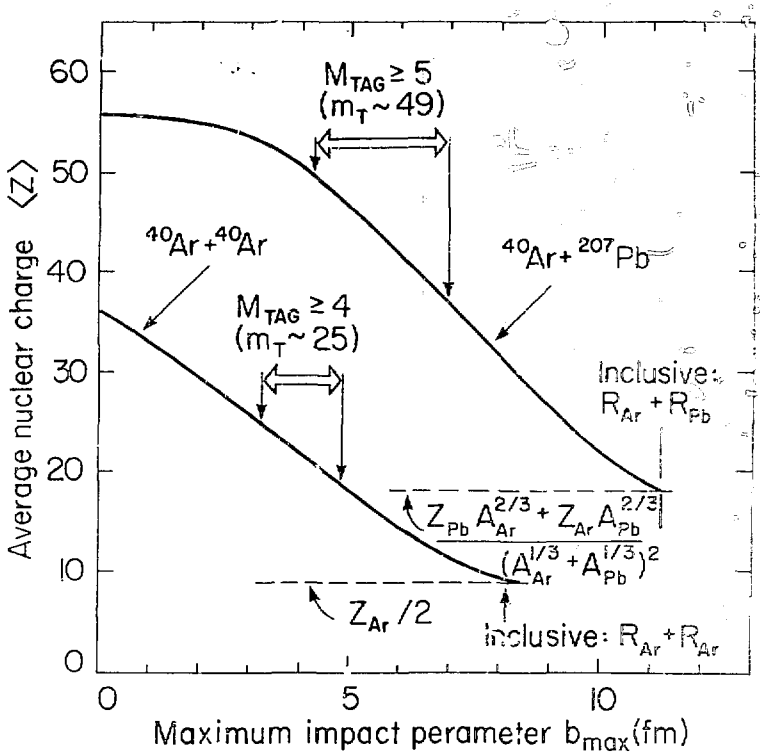
Average nuclear charge ⟨Z⟩
Maximum impact perameter b_{max}(fm)
$M_{TAG} \geq 5$
$(m_T \sim 49)$
$M_{TAG} \geq 4$
$(m_T \sim 25)$
$^{40}Ar + ^{40}Ar$
$^{40}Ar + ^{207}Pb$
Inclusive: $R_{Ar} + R_{Pb}$
$\frac{Z_{Pb} A_{Ar}^{2/3} + Z_{Ar} A_{Pb}^{2/3}}{(A_{Ar}^{1/3} + A_{Pb}^{1/3})^2}$
$Z_{Ar}/2$
Inclusive: $R_{Ar} + R_{Ar}$
XBL 797 2133

Fig. 18

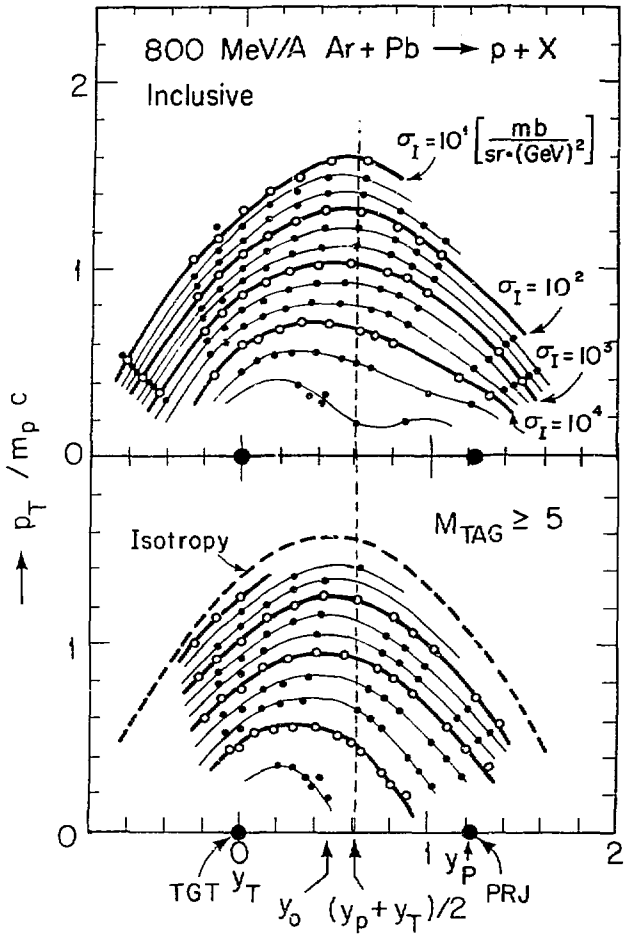
800 MeV/A Ar + Pb → p + X
Inclusive
$\sigma_I = 10^4 \left[\frac{mb}{sr\cdot(GeV)^2}\right]$
$\sigma_I = 10^2$
$\sigma_I = 10^3$
$\sigma_I = 10^4$
Isotropy
$M_{TAG} \geq 5$
$p_T / m_p c$
TGT
y_T
y_o
$(y_p + y_T)/2$
y_P
PRJ
XBL 797 - 2126

Fig. 19

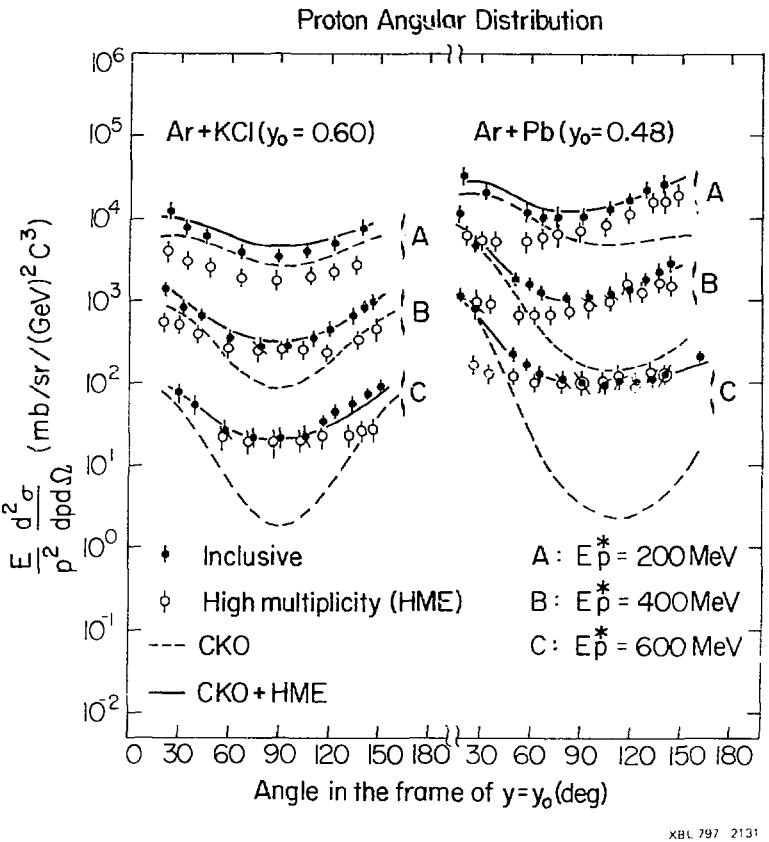
Proton Angular Distribution
Ar+KCl (y_0 = 0.60)
Ar+Pb (y_0=0.48)
A
B
C
$\frac{E}{p^2}\frac{d^2\sigma}{dp\,d\Omega}$ (mb/sr/(GeV)^{2}c^3)
Inclusive
High multiplicity (HME)
CKO
CKO+HME
A: E_p^* = 200 MeV
B: E_p^* = 400 MeV
C: E_p^* = 600 MeV
Angle in the frame of y=y_0(deg)
XBL 797 2131

Fig. 20

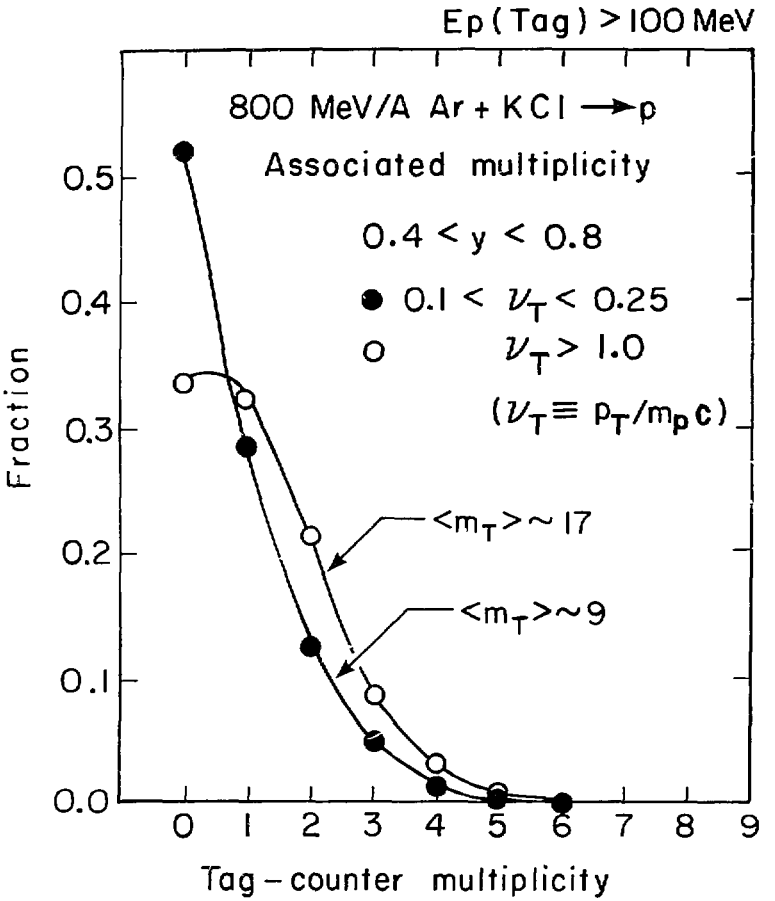

XBL 7810-6626A

Fig. 21

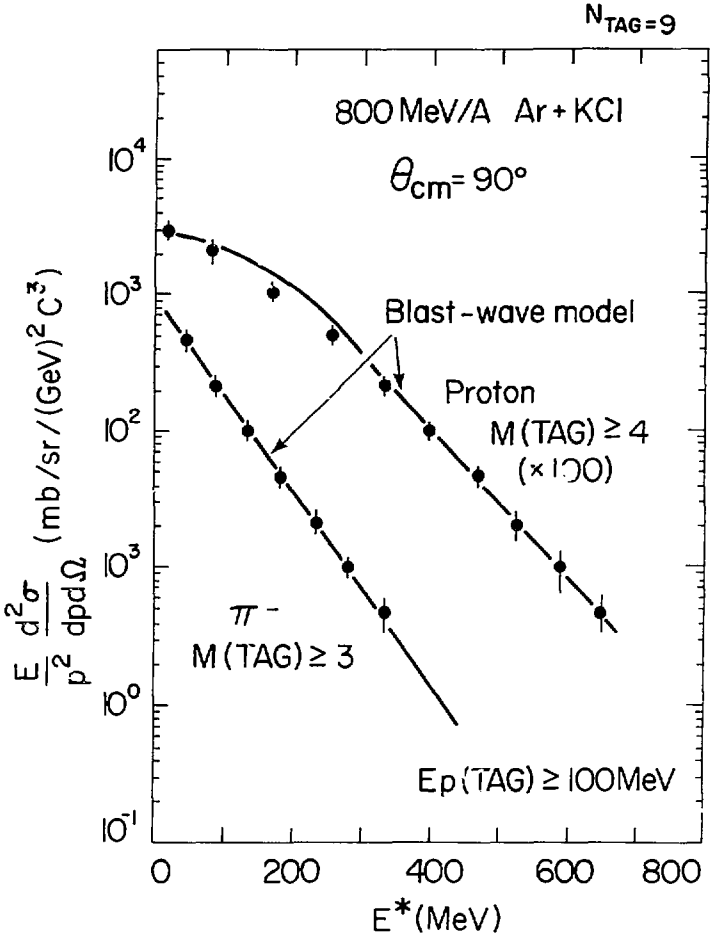

XBL 797 - 2130

Fig. 22

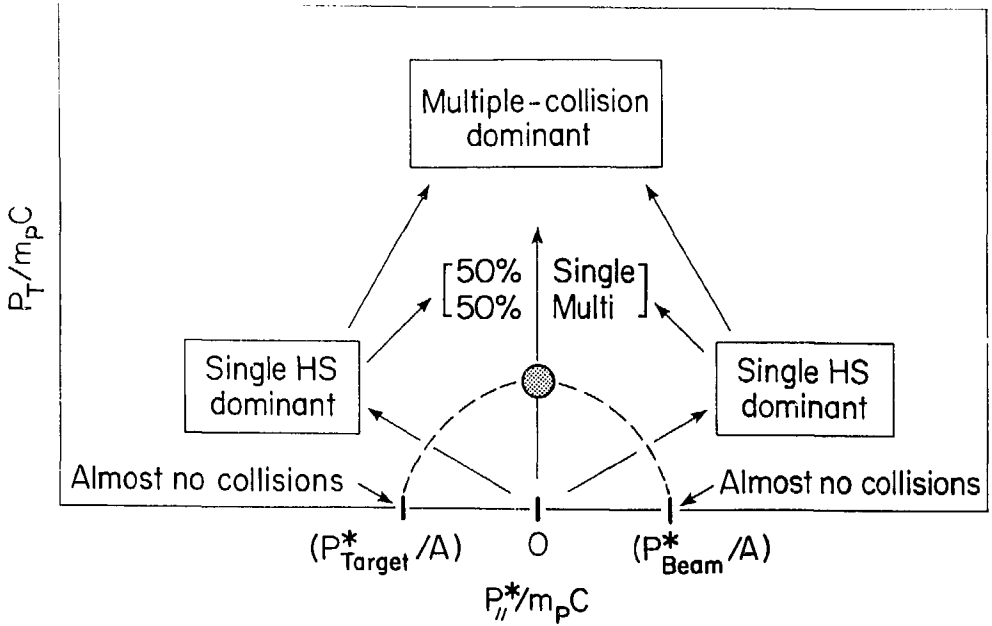

XBL 797 - 2046

Fig. 23

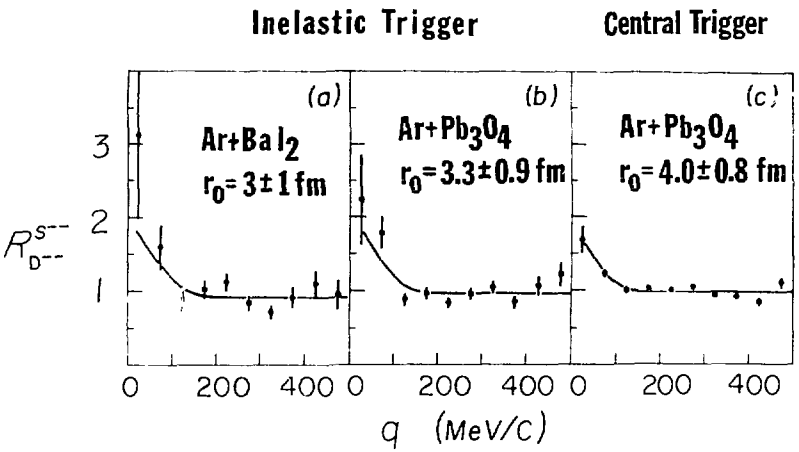
Inelastic Trigger
Central Trigger
(a)
Ar+BaI2
r0= 3±1 fm
(b)
Ar+Pb3O4
r0=3.3±0.9 fm
(c)
Ar+Pb3O4
r0=4.0±0.8 fm
R S-- / D--
3
2
1
0
200
400
q (MeV/C)

Fig. 24

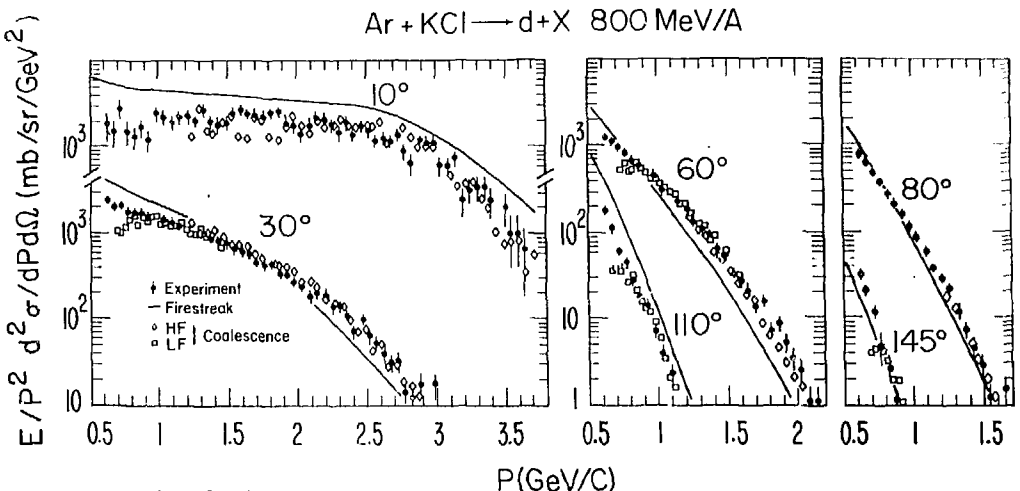

deuteron

(proton)²

Fig. 25

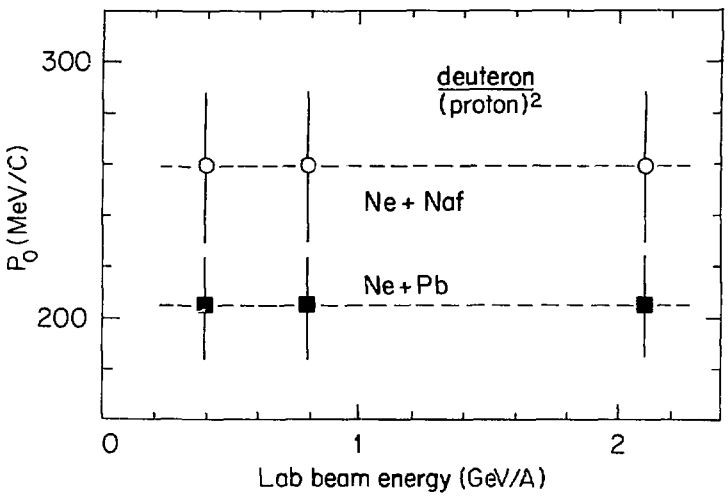

XBL 797 2128

Fig. 26

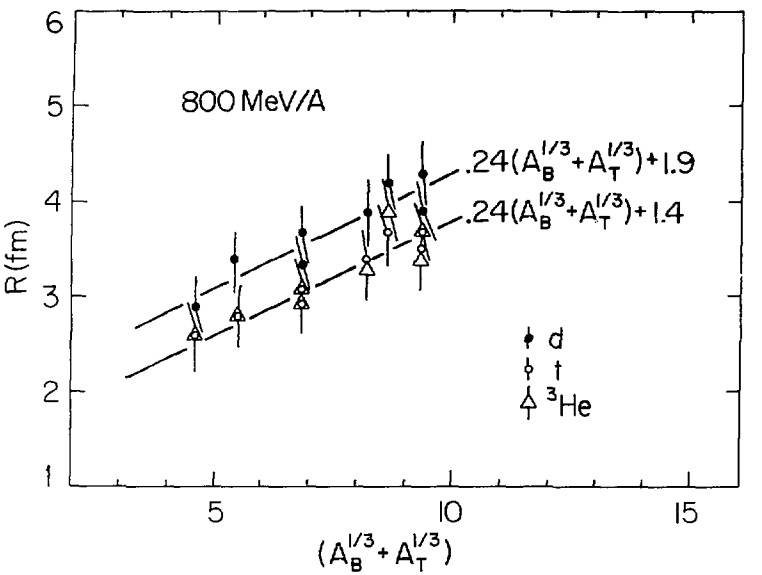

XBL 797 - 2129

Fig. 27

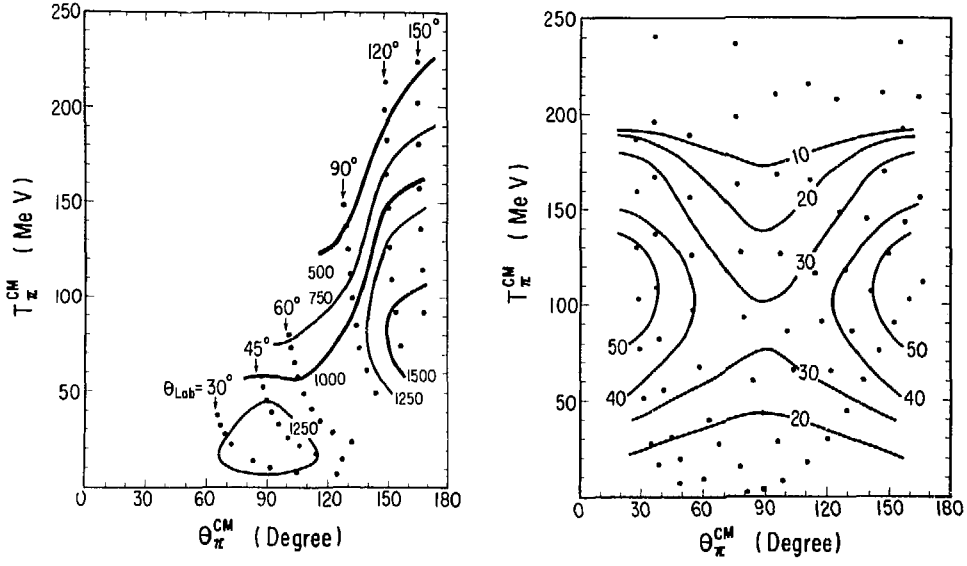

X81. 7812-14103

Fig. 28

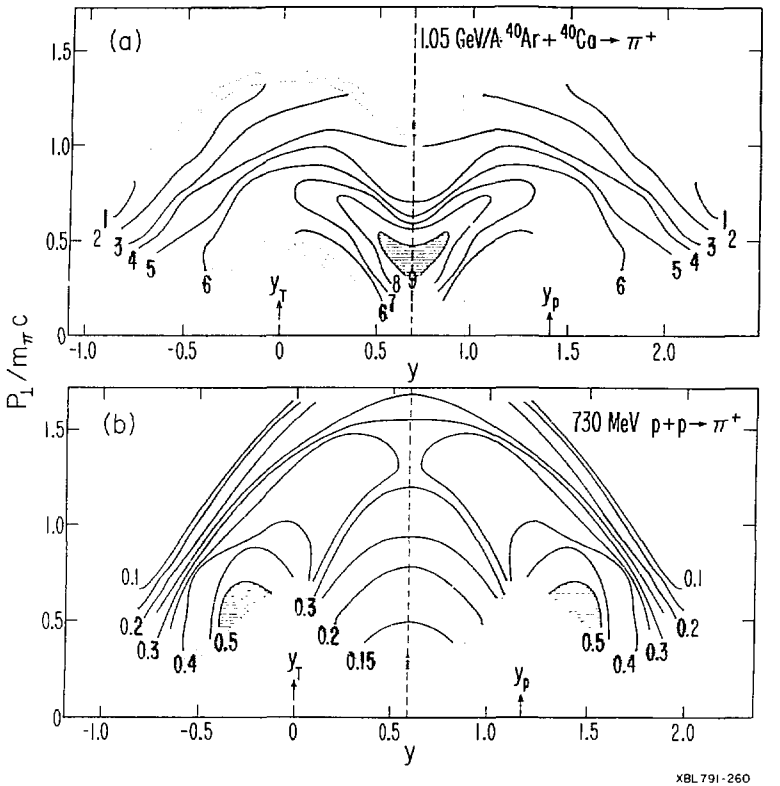
(a)
1.05 GeV/A ^{40}Ar + ^{40}Ca → π^+
(b)
730 MeV p+p → π^+
$P_\perp / m_\pi c$
y
y_T
y_p
XBL 791-260

Fig. 29

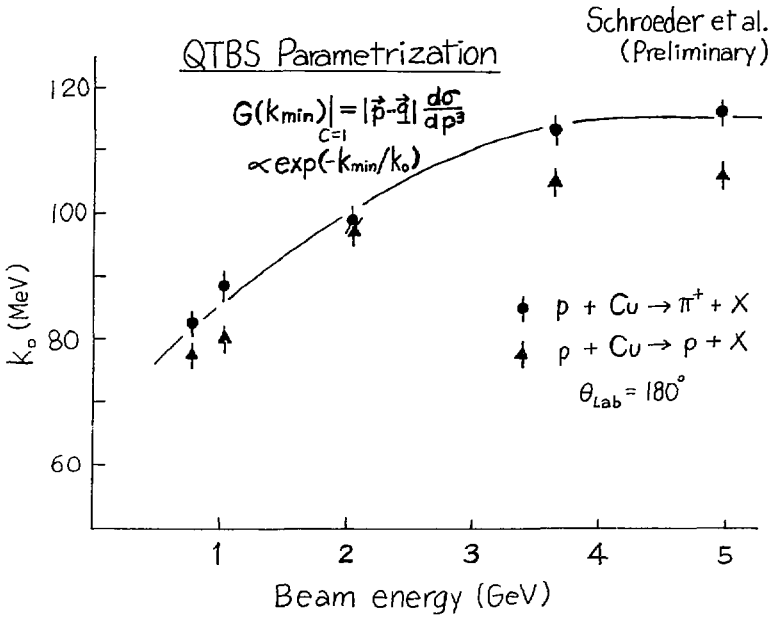

XBL 797-10496

Fig. 30

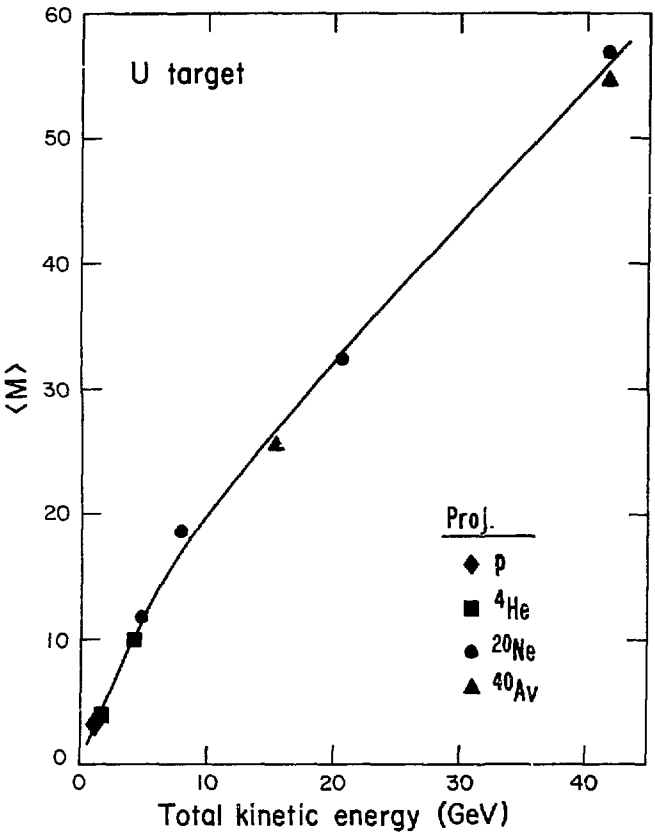

XBL 797 - 2054

Fig. 31

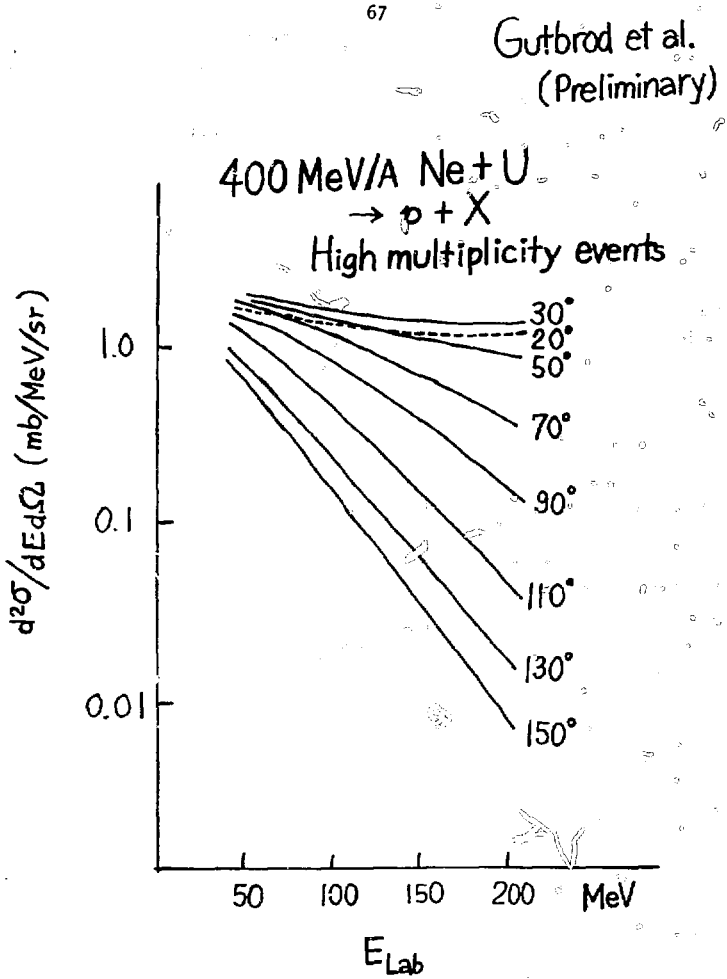

XBL 797-10495

Fig. 32

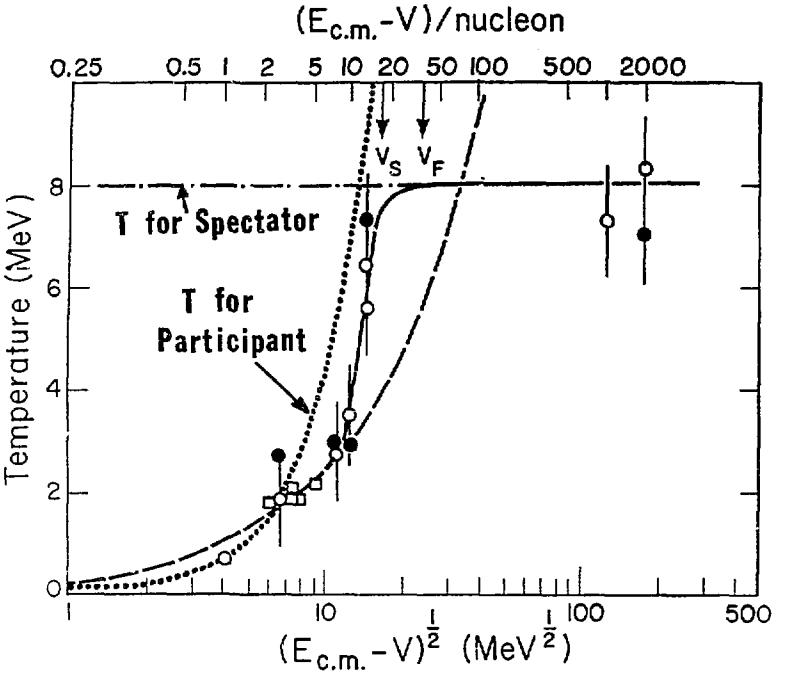
(E c.m.-V)/nucleon
0.25
0.5
1
2
5
10
20
50
100
500
2000
V S
V F
T for Spectator
T for Participant
Temperature (MeV)
8
6
4
2
0
1
10
100
500
(E c.m.-V)^1/2 (MeV^1/2)

Fig. 33

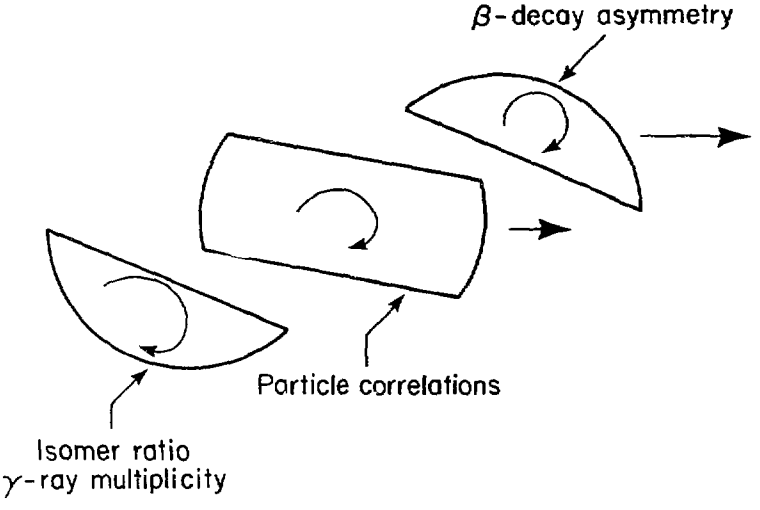

XBL 797 - 2132

Fig. 34